Exploring the Visualisation of the Cervicothoracic Junction in Lateral Spine Radiography using High Dynamic Range Techniques

Presented by:

Quik Kung
KNGQUI001
Division of Biomedical Engineering
University of Cape Town

Supervisor:

Prof. T. Douglas
Division of Biomedical Engineering
University of Cape Town

Co-supervisor:

Dr. S. Dawson
Division of Biomedical Engineering
University of Cape Town

November 2018

Submitted to the Department of Biomedical Engineering at the University of Cape Town in partial fulfilment of the academic requirements for a Master's degree in Biomedical Engineering.

Declaration

I, Quik Kung, hereby declare that the work on which this dissertation is based is my original work (except where acknowledgements indicate otherwise) and that neither the whole work nor any part of it has been, is being, or is to be submitted for any other degree in this or any other university. I empower the university to reproduce, for the purpose of research, either the whole or any portion of the contents in any manner whatsoever.

Signed by candidate

Signature:.....

Quik Kung

09/01/2019

Date:.....

Acknowledgements

I would like to thank Professor Tania Douglas for supervising this project. Without her patience, guidance and tolerance, this project would have never been completed.

Dr. Sarah Dawson, for her help and encouragement throughout.

The NRF as well as UCT's Lodox programme, for their generous financial support, without which, this degree would not have been possible.

UCT's Department of Human Biology - for allowing me to use and construct the phantom for my images.

To Madelein Dreyer and Munya Matose, without them, none of this would have been remotely possible.

Abstract

The C7/T1 junction is an important landmark for spinal injuries. It is traditionally difficult to visualise in a lateral X-ray image due to the rapid change in the bodys anatomy at the level of the junction, where the shoulders cause a large increase in attenuation. To explore methods of enhancing the appearance of this important area, lateral radiographs of a shoulder girdle phantom were subjected to high dynamic range (HDR) processing and tone mapping.

A shoulder girdle phantom was constructed using Perspex, shoulder girdle and vertebral bones and water to reproduce the attenuation caused by soft tissue. The design allowed for the removal of the shoulder girdle in order for the cervical vertebrae to be imaged separately. HDR was explored for single and dual-energy X-ray images of the phantom.

In the case of single-image HDR, the HDR image of the phantom without water was constructed by combining images created with varying contrast windows throughout the contrast range of an X-ray image. It was found that an overlap of larger contrast windows with a lower number of images performed better than smaller contrast windows and more images when creating an HDR to be tone mapped. Poor results on the phantom without water precluded further testing of single-image HDR on images of the phantom with water, which would have higher attenuation.

Dual energy HDR image construction explored images of the phantom both with and without water. A set of images acquired at lower attenuation (phantom without water) was used to evaluate the performance of the various tone mapping algorithms. The tone mapping was then performed on the phantom images containing water. These results showed how each tone mapping algorithm differs and the effects of global vs. local processing. The results revealed that the built-in MatLab algorithm, based on an improved Ward histogram adjustment approach, produces the most desirable result. None of the HDR tone mapped images produced were diagnostically useful.

Signal to noise ratio (SNR) analysis was performed on the cervical region of the HDR tone mapped image. It used the scan of the phantom without the shoulder girdle obstruction (imaged under the same conditions) as a reference image. The SNR results quantitatively show that the selection of exposure values affects the visualisation of the tone mapped image. The highest SNR was produced for the 100 - 120 kV dual energy X-ray image pair.

The study was limited by the range of HDR image construction techniques employed and the tone mapping algorithms explored. Future studies could explore other HDR image construction techniques and the combination of global and local tone mapping algorithms. Furthermore, the phantom can be replaced by a cadaver for algorithm testing under more realistic conditions.

Contents

List of Figures

List of Tables

Chapter 1

Introduction

1.1 Background

In South Africa, both sporting and motor accidents occur at a high rate. Directly related to these are injuries and trauma. According to Statistics South Africa, in 2016, transport accidents were responsible for 12.5% of all non-natural causes of death (StatsSa, 2018). Spinal injuries often occur as a consequence of these.

The cervical region of the spinal cord, as the name suggests, involves the neck region and, in the aforementioned trauma situations, its evaluation is a critical responsibility of the trauma team (Kulaylat et al., 2012). The cervicothoracic junction (the junction between the last cervical and first thoracic vertebrae) is an important landmark for injuries due to its abrupt change in anatomy and biomechanics (Mullin et al., 2013).

The cervicothoracic junction acts as an important landmark for injuries and is a vital point for clinical analysis. It thus is a vital criterion for a successful lateral radiograph (Mullin et al., 2013). Currently, lateral scans do not provide a reliable way to view the junction (Kulaylat et al., 2012; Fell, 2010; Mullin et al., 2013; Rethnam et al., 2008). The susceptibility of this junction to injury creates a need for an efficient and reliable technique for its radiographic visualisation.

Although a visible cervicothoracic junction is a requirement for a successful lateral scan, such scans often do not produce a clear image (Kulaylat et al., 2012; Fell, 2010; Mullin et al., 2013; Rethnam et al., 2008). This project explores ways of improving the cervicothoracic junction.

Despite advances in radiographic technology, visualising the cervicothoracic (C7/T1) junction of the vertebrae with lateral spine radiography is still challenging (France et al., 2005). Medical imaging advances in both Magnetic Resonance Imaging (MRI) and Computed Tomography (CT) have provided alternate means to visualise the junction. A CT image outperforms a radiograph in accuracy, diagnostic ability and trauma analysis of the lateral cervical spine (France et al., 2005; Parizel et al., 2009; Como et al., 2011).

However, a CT is not more efficient or easier to perform than a radiograph. Putting a critical patient into a CT presents a greater clinical risk than X-ray imaging would. Furthermore, CT imaging is not always available in the South African context. In the public health care sector, there were 10 reported available CT scanners in 2012, with the largest concentration in Gauteng Province (Necsa, 2012). Furthermore, the costs of CT and MRI are much higher than that of radiography (Como et al., 2011; France et al., 2005; Parizel et al., 2009). Taking these factors into consideration, it becomes clear that in South Africa, radiography remains relevant in trauma imaging. This is also the case in other developing countries.

1.2 Research Aim and Objectives

The aim of the research was to explore the ability of High Dynamic Range (HDR) image processing techniques to enhance the C7/T1 junction on lateral cervical spine images obtained using the Lodox X-ray imaging system. The objectives were to:

- Design and construct a phantom that mimics the C7/T1 junction.
- Implement HDR techniques on images of the C7/T1 junction.
- Assess the effectiveness of HDR in improving C7/T1 visualisation.

1.3 Document Outline

Chapter 2 contains the literature review. It gives an overview of X-ray images and attenuation. The current methodologies of C7/T1 X-ray imaging and high dynamic range imaging are then introduced along with the tone mapping used within the HDR methodologies. This is followed by a review of a dual exposure technique used for dynamic range extension.

Chapter 3 provides the research methodology, including the design of a phantom and the HDR methods employed. Chapter 4 provides the results of the HDR implementation. Conclusions regarding the effectiveness of these methods for exploring the visualisation of the C7/T1 junction are drawn in Chapter 5 and recommendations are made for further work.

Chapter 2

Literature Review

In this chapter the basics of X-ray attenuation and its effect on medical imaging and the imaging of the cervicothoracic junction on the spinal cord are discussed. The current solutions to C7/T1 visualisation are discussed along with their advantages and shortfalls. High dynamic range (HDR) imaging is then introduced and reviewed and its medical applications are discussed.

2.1 X-ray Attenuation

In radiology and all medical imaging of the human body, energy that is capable of penetrating and interacting with the tissue is used in order to produce an image (Bushberg et al., 2002). Radiography is performed by emitting X-ray radiation from a source, through the patient towards a detector. The X-rays are partly absorbed and partly scattered by the irradiated object (Carlsson and Carlsson, 1996). That is, a photon's energy has either been absorbed or its direction of motion changed. In terms of mono-energetic photons, the intensity removed or scattered when incident on a material is proportional to the intensity of incident photons and the thickness of the material. This is shown in equation 2.1, where I is the intensity of incident photons, x is the thickness of material and μ is the linear attenuation coefficient (Bushberg et al., 2002).

$$dI = -\mu I dx \tag{2.1}$$

The linear attenuation coefficient is defined as the probability of a photon from a given wavelength and a given energy level interacting while passing through a given medium.

Different interactions add their individual contributions to the total attenuation. The solution to the differential equation in equation 2.1 is:

$$I(x) = I(0) \times e^{-\mu x} \tag{2.2}$$

Equation 2.2 shows that the primary photons are exponentially attenuated with depth of penetration. Consider mass thickness, m, defined as mass per unit area, which can be obtained by multiplying density (ρ) and thickness (x) (Hubbel and Seltzer, 2009) :

$$m = \rho \times x \tag{2.3}$$

With equation 2.3, equation 2.2 can be rewritten in terms of mass thickness:

$$I(x) = I(0) \times e^{(-\mu/\rho)m} \tag{2.4}$$

The mass attenuation coefficient (μ/ρ) is then:

$$\mu/\rho = \frac{\ln\left(\frac{I(0)}{I(x)}\right)}{m} \tag{2.5}$$

For mixtures or compounds, the mass attenuation coefficient is obtained by addition of the mass attenuation coefficient of each substance:

$$\mu/\rho = \sum_i w_i \left(\frac{\mu}{\rho}\right)_i \tag{2.6}$$

where w is the weight fraction of the i^{th} atomic constituent. The mass attenuation coefficient is a basic quantity used to calculate the penetration of photons in X-rays or γ-rays in biological or shielding materials (Hubbel and Seltzer, 2009).

An X-ray image shows the variations in the transmissions caused by the structures that the irradiated object/patient is made up of. These include the thickness, density and atomic composition which allow for bone to be viewed in good contrast to surrounding soft tissue (Carlsson and Carlsson, 1996).

2.2 X-ray imaging of the Cervicothoracic Junction

The spinal cord is made up of five separate regions, each with different numbers of vertebrae. These are, from superior to inferior, the cervical (7), thoracic (12), lumbar

(5), sacral (5) and coccygeal (4) vertebrae. The cervical region of the spinal cord, as the name suggests, involves the neck region and its evaluation is a critical responsibility of the trauma team (Kulaylat et al., 2012). The imaging of patients with a suspected cervical spine injury is done using three radiographs (Fell, 2010). These are:

- Odontoid
- Anterior-posterior
- Lateral

This assessment is a component of the secondary general trauma survey and is performed when the patient's airway and hemodynamic status is stable. Focusing on a lateral cervical scan, an acceptable radiograph consists of (France et al., 2005):

1. Non-rotated, true lateral view provided there is no rotational injury.
2. The basion[1] and opisthsion[2] can be identified.
3. Visualisation of the cervicothoracic junction[3], disk space and facet joints.
4. Visualisation of the occipitocervical junction[4].
5. Visualisation of the spinous process of each cervical vertebra.

With adequate lateral, antero- posterior and odontiod radiographs, successful visualisation of the C7/T1 junction has been reported in up to 99% in a single group (MacDonald et al., 1990). However, this requires three successful scans. One of the three scans, a single lateral scan, having a 73% success rate in a single group thus skews the reported 99% success rate as an inaccurate depiction of the C7/T1 visualisation (France et al., 2005; Parizel et al., 2009). Lateral cervical radiographs produce a high false-negative rate, which creates the requirement of the anteroposterior and odontiod radiographs (France et al., 2005).

The challenge in visualising the cervicothoracic junction is due to the abrupt change in thickness at the level of the junction between the neck and the shoulder, as indicated by Figure 2.1. The penetrating radiation from a single lateral radiograph is unable to

[1]Anterior aspect of foramen magnum.
[2]Posterior aspect of foramen magnum.
[3]Between the seventh cervical and first thoracic vertebra.
[4]Between the first cervical vertebra and the occipital.

produce an image of the spinal cord with adequate visualization of the region surrounding the junction. This is because the energy of the scan is set either correctly for the thin part of the soft tissue, thus not penetrating the thicker parts, or for the thick part and thus overexposing the parts without sufficient attenuation (France et al., 2005).

Various radiographic solutions to better visualise the C7/T1 junction have been explored (Fell, 2010; Kulaylat et al., 2012; France et al., 2005). The swimmer's projection and supine oblique techniques are popular solutions in practice.

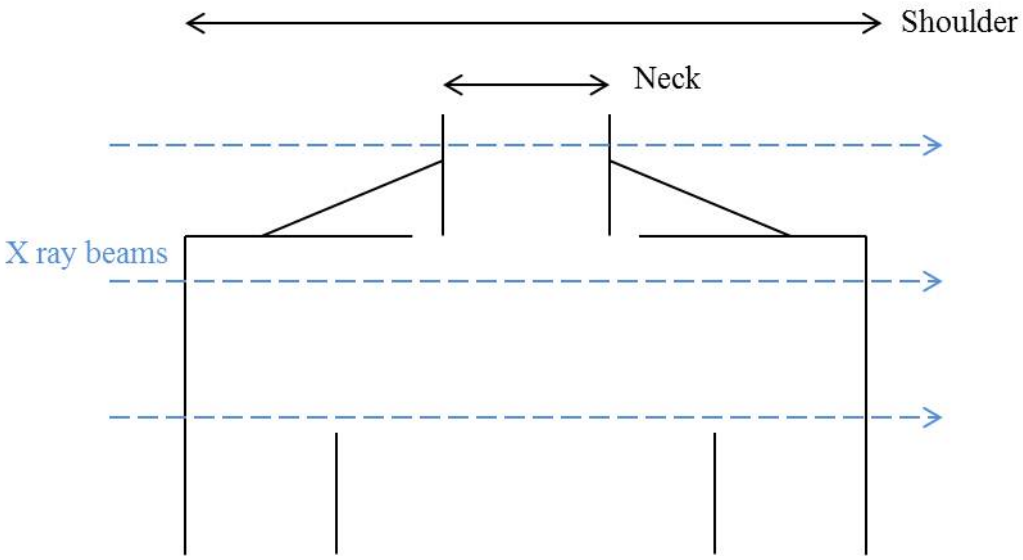

Figure 2.1: Basic illustration of the upper body and the sudden change in thickness from the neck to the shoulder.

The swimmer's projection places the patient in a free-style like position prior to imaging. This can be achieved in both a standing and a lying position, as illustrated in Figure 2.2. The goal of this technique is to evenly distribute the soft tissue volume from the surface of the body to the vertebrae (Ahmad, 2003). This increase in tissue volume requires an increase in radiation dosage as compared to that of a conventional lateral scan (Fell, 2010). The projection requires the patient to extend the shoulder joint, a movement that involves the upper limb and a shift in position of the cervical and thoracic vertebrae. Considering a patient with a suspected neck injury or an unknown/undiagnosed trauma scenario, this movement creates unnecessary risks of further injury. This risk is not justified given the unreliability of the produced images (Fell, 2010).

A supine oblique scan is obtained by projecting the radiation beam at an angle to the patient (Wheeless, 2011). Placing the incident ray at an angle effectively avoids the abrupt change at the C7/T1 junction and exposes it to evenly dispersed tissue volumes. Two obvious methods of obtaining these scans are: rotation of the beam source or rotation

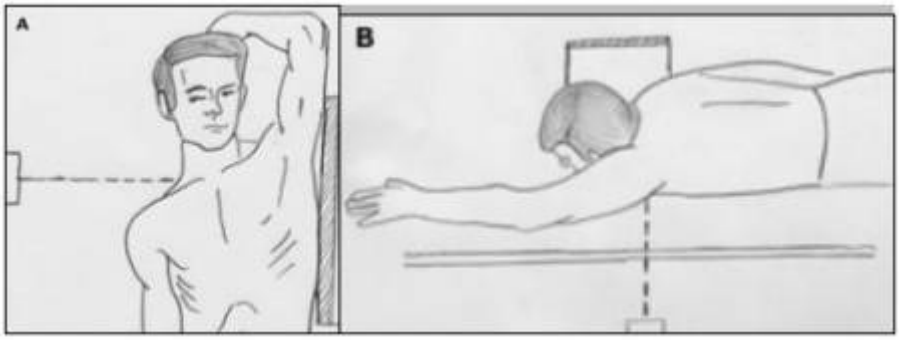

Figure 2.2: Illustration of the swimmers projection pose in a standing and lying position (Ahmad, 2003).

of the patient. The shortcoming of this technique is the requirement for a mobile beam source, implying increased costs. Rotating the patient implies an increased risk of further injury, particularly in cases of spinal injuries. Fell (2010) conducted a survey which showed that professionals opted for a swimmer's projection X-ray image followed by computed tomography (CT) if the X-ray image gave insufficient information. CT was preferred to the supine oblique scan, which was found to be difficult to interpret and lacked information.

2.2.1 Computed Tomography

The popularity of CT scans to visualise possible cervical spine injuries has increased in recent years (Fell, 2010). CT outperforms radiographs in accuracy, diagnostic ability, efficiency and trauma analysis of the lateral cervical spine (France et al., 2005; Parizel et al., 2009; Como et al., 2011).

Given the disadvantages of X-rays, many institutions are either using CT as part of the primary imaging approach in high risk patients with traumatic injuries or insist on a CT after a suspected injury is detected in the lateral X-ray image. This is done for better diagnostic ability, in particular for fracture assessment and treatment plans (France et al., 2005; Parizel et al., 2009).

CT has better accuracy and diagnostic ability compared to conventional radiography and has experienced an improvement in speed and efficiency with technological advances. The increase in speed is largely due to the introduction of the spiral/helical CT and the multidetector CT (MDCT), which are refined techniques used to allow for rapid data acquisition for diagnostics (Parizel et al., 2009).

Despite the advantages, a CT exposes the patient to an increased radiation dose. The approximate risks of fatal cancer directly related to radiation exposure by a lateral X-ray scan is 1 : 1000000 (Fell, 2010). The risk from a CT scan is 1 : 9000. A patient should consider a CT when the C7/T1 or occipitocervical junctions are not visible in radiographs or when an injury is detected in the radiograph and requires further analysis (France et al., 2005).

Although CT has advantages compared to traditional radiography, X-rays still play a major role in trauma settings. In the public sector of South African health care, there were only 10 reported available CT scanners in 2012, with the largest concentration in Gauteng (Necsa, 2012). Furthermore, the costs of CT is much higher than that of radiography (Como et al., 2011; France et al., 2005; Parizel et al., 2009). Taking these factors into consideration, it becomes clear that, particularly in South Africa, radiography still remains highly relevant in trauma and medical imaging of the lateral cervical spine.

2.3 High Dynamic Range Imaging

Dynamic range is defined as the luminance ratio between the brightest and the darkest object within an image (Meylan, 2006; Devlin, 2002). Luminance is defined as the amount of light given off a surface per unit area. An image is said to have HDR if the dynamic range exceeds that of the display device. An HDR image is an image type that attempts to capture and store the extended range and information found in the ranges outside that of display devices. The benefit of this image is that the stored information within it that is outside the visual range of a traditional display device can be combined that can be visualised into an image by a process called tone mapping.

In an ideal scenario, an image should not be constructed by bits, but rather by a mathematical or parametric representation of the continuous varying intensities of light projected onto a plane (Mann and Picard, 1994). This allows for the intensities within the image to vary depending on the light or other conditions described by the parameters. An approximation of this ideal representation for a digital image is done by the multiple exposure principle as shown in Bandoh et al. (2010) and Mann and Picard (1994). The multiple exposure principle is the technique used to construct the HDR image.

The multiple exposure principle takes multiple images of still objects at a fixed location at various exposure values. The camera's response curve - a function that relates the amount of light entering the camera and the image pixel value - is then estimated and the multiple

exposures for the entering light are self calibrated. This non-linear pixel value/quantity is set by the camera response function which varies between products (Reinhard et al., 2006). Various techniques to estimate this function include gamma functions, sets of exposure values and low order polynomials (Bandoh et al., 2010; Mann and Picard, 1994; Debevec and Malik, 1997; Mitsunaga and Nayer, 1999). The estimated function can be used for all images taken with the same camera provided the camera response function is constant. The exposure settings are calibrated according to this response curve.

Each image with the response curve is then linearised in order to factor out the different exposures and put each pixel in the image in the same unit of measurement. This linearisation is required in order to undo the non-linear response curve such that each image can then be merged into the HDR image (Reinhard et al., 2006). The linearisation is achieved by applying the inverse of the response curve , and then averaging them into a single HDR image (Granados et al., 2010)

The basic steps in HDR image acquisition are:

1. Digital images of still objects taken are taken at a fixed location.
2. The camera response curve is estimated and multiple exposures are set by self calibration.
3. Images are linearised by applying the inverse of the response curve.
4. Linearised images are merged.

Most differences in HDR algorithms occur during the response curve estimation. Modern cameras determine the colour value Z at pixel i by combining the radiance E on the sensor and the exposure time Δt, that is:

$$Z_i = f(E_i \Delta t) \tag{2.7}$$

Debevec and Malik (1997) determined the inverse of the camera response function with the objective function found in Equation 2.8.

$$O = \sum_{i=1}^{N} \sum_{j=1}^{P} \{w\left(Z_{ij}\right)\left[g\left(Z_{ij}\right) - lnE_i - ln\Delta t_j\right]\}^2 + \lambda \sum_{z=Z_{min}+1}^{z_{max}-1} \left[w(z)g^{''}(z)\right]^2 \tag{2.8}$$

g is the natural logarithm of the (invertible) camera function, Z_{min} and Z_{max} are the pixel value boundaries, N is the number of samples, P is the number of photographs/images and w is a weighting function to ensure a smooth function g (Webb, 2008; Debevec and Malik, 1997). Once g is fully determined, an HDR radiance map can be constructed. The radiance map is reconstructed by combining the exposures, that is the weighted average of the response function of the pixels in each exposure (Webb, 2008). This is shown in Equation 2.9 where N now depicts the number of pixels in each image.

$$lnE_i = \frac{\sum_{j=1}^{P} w(Z_{ij})(g(Z_{ij}) - ln\Delta t_j)}{\sum_{j=1}^{P} w(Z_{ij})} \tag{2.9}$$

The HDR image can now be created and will contain more information than can be traditionally displayed. However, this HDR needs to be processed into an image that can be viewed whilst containing all useful information within the image. This process is referred to as tone mapping.

2.3.1 Tone Mapping

A process called tone reproduction, or tone mapping, is required to compress an HDR image into a narrow enough or low dynamic range (LDR) in order to be displayed (Devlin, 2002; Meylan, 2006). This process retains the localised contrast (Lakshmi et al., 2012). Tone mapping can be split into two broad categories: global and local. Global operators apply compression on the whole image while local uses varying compression ratios for different parts of the image (Salih et al., 2012). Simple tone mapping algorithms compress the dynamic range using logarithmic, gamma or sigmoidal functions (Meylan, 2006) which mostly act on the HDR images' luminance channel as this largely depicts the human perception of contrast (Webb, 2008). Algorithms range from linear scaling (simplest) to complex global and local tone mappings to prevent discrepancies such as halo effects (Webb, 2008; Meylan, 2006). Common global operators include the Ward and Drago whilst local include Durand, Ashikhmin and Reinhard algorithms (Yoshida et al., 2005).

The Ward or histogram adjustment tone mapping operator (Larson et al., 1997) provides contrast compression for pixels in sparsely populated regions of the image histogram (Yoshida et al., 2005). This overcomes the dynamic range shortage and leads to a monotonic tone reconstruction curve which is applied globally. The curve is constrained as to not exceed the contrast perceived in a real scene by the human eye (Yoshida et al., 2005).

Reinhard et al. (2002) introduced a tone reproduction technique inspired by photographic film development and printing. An initial global tone map function is used to compress the luminance to a displayable range. The image quality is then enhanced locally by using a photographic dodging and burning technique - a technique that allows for different exposures to be applied to each part of the image (Yoshida et al., 2005). This process has been automated by finding the low contrast regions using a center-surround function at different scales (Reinhard, 2003). A local tone map function is then applied, followed by an automatic dodging and burning method to enhance contrast and details whilst preserving the luminance characteristics.

Lischinski et al. (2006) introduced an automated local tone mapping algorithm which decomposes an image into different zones, each with an appropriate exposure value. Each pixel in then associated with this target value. In order to prevent discontinuity between zones, the pixels are placed under a soft constraint for the solver (Lischinski et al., 2006). The number of zones is determined by:

$$Z = [log_2(L_{max}) - log_2(L_{min} + \epsilon)] \tag{2.10}$$

A luminance value R_z is then chosen for each zone$z$ and is then mapped to a target value $f(R_z)$. The function f is a parameter map resulting from a set of defined constraints Lischinski et al. (2006). The final exposure is then $log_2(f(R_z)/R_z)$.

Three main methods of tone mapping have been discussed, each with their own pros and cons. The key difference lies in the global or local applications of each algorithm. Global applications create a lower contrast but smoother image overall whereas the local algorithm creates sharper contrast differences between pixels and thus an image with sharper changes. Global algorithms create an image that is easier to view and a local algorithm brings out sharper detail.

2.4 HDR in Medical Imaging

HDR imaging and tone mapping have been applied in the medical field. Applications include optical coherence tomography, dental and hip radiography and mammography. Furthermore, the dynamic range of X-ray images has been extended with the use of dual exposures. These applications and solutions are explored in the following sections.

2.4.1 Optical Coherence Tomography in Ocular Tissue

Optical coherence tomography (OCT) is a non-invasive and non-contact imaging technique that has been used, among other applications, to generate in vivo, cross-sectional images of the ocular tissue with microscopic resolution through the measurement of interference of the reflected signal from the posterior of the eye (Ishikawa et al., 2013). The ability to interpret and analyse these OCT images is affected greatly by the variability in signal quality. HDR has been applied to OCT images to compensate for signal differences for both a qualitative and quantitative assessment (Ishikawa et al., 2013).

The HDR method adopted consists of two steps. Step one is the processing of three virtual OCT signals. The technique adopted divides a single OCT image into three "virtual" 8 bit data sets by distributing the image contrast histogram in order to mimic the multiple exposures used in traditional HDR. The datasets effectively create three images. This stretching allows for maximised tissue visualisation.

Step two is the HDR signal composition. The virtual OCT signals are further broken into four groups based on Stein et al. (2006). These groups are based on the minimum, maximum, noise and saturation level. These values are used to divide the OCT dataset into three separate datasets - low (I_{low}), middle (I_{mid}) and high (I_{high}). These signals are created by incorporating the following offset values:

$$\text{Offset}_{Low} = \text{Noise} + 0.23 \times (\text{Saturation} - \text{Noise}) \tag{2.11}$$

$$\text{Offset}_{High} = \text{Saturation} - 0.067 \times (\text{Saturation} - \text{Noise}) \tag{2.12}$$

Each dataset is then further processed to enhance the dynamic range by rescaling it to lie between 0 and 255, or an 8-bit gray scale range. These signals are then combined using step two, the HDR signal composition. The signal is reconstructed using the following equation:

$$I_{HDR}(x,z) = \frac{1}{C_L + C_M + C_H}(C_L \times I_{Low}(x,z) + C_M \times I_{Mid}(x,z) + C_H \times I_{High}(x,z)) \tag{2.13}$$

where I_{HDR} is the output HDR image, (x, z) indicates the position and pixel values, that is the x^{th}-scan in the z^{th} pixel in the axial direction. C_L, C_M and C_H are weighted coefficients used to calculate the weighted mean and are adjusted as according to original signal strength.

The image appearance is objectively analysed by using a modified signal-to-noise (SNR) and contrast-to-noise (CNR) ratio.

Stein et al. (2006) finds that the HDR technique successfully reduced the variability in signal quality in a wide range of signal strengths as compared to the measurement variability obtained at a good signal strength. The image quality in areas with moderately poor signal quality were also enhanced, effectively reducing signal variability. The algorithm is unable to compensate for extremely low signal quality. However, such low signal quality levels are clinically rare in the ocular tissue application.

Despite the successful restoration of signal and image quality, this method adopted by Stein et al. (2006) was not strictly HDR as it employed virtual HDR data. However, the stretching of a segmented single image into virtual exposures effectively stretches the image's dynamic range, thus achieving an HDR result.

2.4.2 Dental Radiography

In modern dentistry, digital radiographs are commonly used for orthopantogram[5] and cephalometric[6] views (Trpovski et al., 2013). For the cephalometric view, the patient's head is held in a cephalostat, thus drastically limiting the movement of the head. The scan is then done at an energy level determined by the radiologist (Trpovski et al., 2013). With an energy level too low, radiographs appear bright with partly invisible bone details. An energy level too high creates a dark radiograph and again, little to no detail can be

[5]Dental panoramic radiograph of upper and lower jaw.
[6]Lateral radiograph of head, including mandible.

observed. Trpovski et al. (2013) used an HDR processing algorithm to combine an over- and under-energised radiograph into a usable and diagnostically useful image.

The HDR images were generated with the Matlab HDR Toolbox and the algorithm adapted for grayscale X-rays. The modification eliminates the repeated calculations followed for the three RGB planes. The same process was followed for the tone mapping algorithms. Furthermore, the exposure value required for the HDR algorithm was calibrated by a general calibration formula that functions for all radiographs.

The research, conducted on skulls, followed the procedure listed below:

1. Human skull radiograph is taken.
2. A radiologist manually selects the most legible skull radiograph for orthopantogram and cephalometric views.
3. Maximum and minimum energy (as determined by the imaging device) images are taken of the same skull.
4. Exposure calibration is performed to determine exposure value for HDR algorithm of each radiograph.

Trpovski et al. (2013) showed that two images of poor quality processed with the HDR algorithm produced a diagnostically useful image. The method also produced more information than a single scan did, albeit at a much higher radiation dosage due to increased number of scans. Figure 2.3 shows an example of how a referent X-ray (as chosen by radiologist) compares to an HDR combined image and shows the difference between the two. Tone mapping was restricted to global algorithms. Local algorithms were believed to produce visually good but medically less useful images due to increased contrast with increased noise. The Gamma, Drago and Reinhard operators achieved the best results, as judged by the radiologist. Clinical validation was not done in this study.

2.4.3 Hip X-ray images

Valuable medical information, captured in the absence of modern digital radiography and stored on film radiographs, can be lost because of the large dynamic range within the radiograph but limited visible range of traditional viewing devices. Photographic images of film radiographs and the HDR imaging technique have been used by Florea et al. (2007)

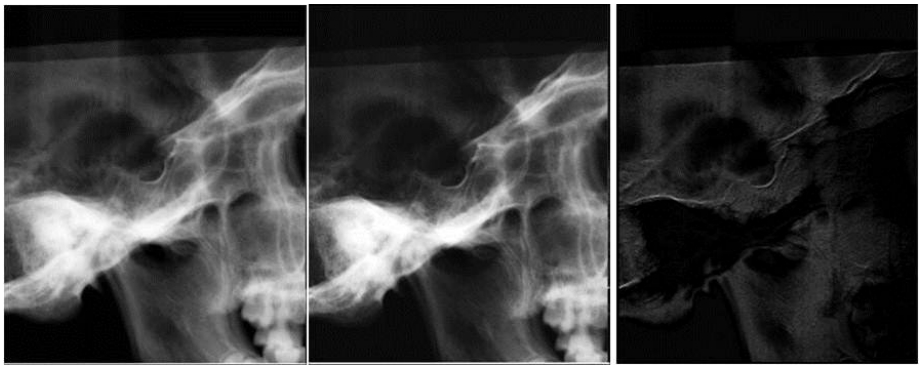

Figure 2.3: *Left to right* - Referent image, HDR generated image and the difference between the two (Trpovski et al., 2013).

in an attempt to ensure minimal loss of information from film radiographs. This method reverted back to the classical camera exposure variation used for HDR, that is multiple images at different exposures in order to extend the dynamic range. The implementation consisted of image registration; camera response function (CRF) estimation and image combination.

Image registration was achieved by using the global matching method of spectrum phase correction. This method uses the translation property of the Fourier transform, that is, for non-aligned images, the corresponding shift to achieve maximum alignment will be the maximum difference in the phase spectrum. The CRF is the mapping of the recorded brightness on the device to the radiance of the actual scenes. As explained in §2.3, the CRF can be obtained using a set of differently exposed images. However, a simpler approach was taken by Florea et al. Modern digital still cameras are capable of estimating the deviation of an image from the ideal exposure value. Thus, a confidence level for each exposure value was computed for multiple images taken under identical physical conditions.

The simple approach of fusing a set of N frames taken using a digital camera under several exposures was used. The saturated pixels were discarded and the remaining values averaged. Due to the varying exposure, a correction factor, the exposure factor (EV) was required. The resultant image was obtained using the following equation:

$$f_{HDR}(l,m) = \frac{1}{N_0} \sum_{i=1}^{N_0} 2^{EV(i)} f_i(l,m) \tag{2.14}$$

where N_0 is the number of non-saturated frames, and l and m are the pixel coordinates.

Classical and homomorphic logarithmic image processing (LIP) was also performed on the HDR images. The classical LIP increases the visibility of objects in dark areas and prevents pixel saturation. The homomorphic LIP is based on the work done by Patrascu et al. and bounds the grey-tone values of the involved images onto a standard $(-1, 1)$ set. The advantage of implementing a logarithmic image fusion is the increased dynamic range of the resultant images.

This implementation increased the number of different brightness levels. The results of the four different approaches undertaken (averaging, CRF weighted average, classical addition and multiplication, LIP methods) were evaluated based on the ability to observe details of a prosthesis in a hip joint and the surrounding bone. The images produced by the homomorphic LIP exhibited the highest increase in dynamic range. This method successfully enhanced the dynamic range, increasing the number of grey levels within images of a film radiograph of a hip-prosthesis obtained from a consumer digital camera.

2.4.4 Mammography

Mammography is an X-ray examination of the breast for cancer. Mammograms have a high dynamic range consisting of a 12 - 14 bit grayscale resolution, however, common display devices are limited to low dynamic ranges, creating a low contrast mammogram (Kanelovitch et al., 2013). Kanelovitch et al. implemented a compression system of the dynamic range to bring the image into a suitable, displayable range with improved contrast and visibility of details within the image. The authors called their method the biologically derived mammography companding (BDMC) algorithm.

The BDMC consists of two main parts: preliminary and HDR companding. Initially, the preliminary stage aims to reduce HDR processing time by removing the areas not involved in the breast. This is followed by an intensity standardisation, to standardise the vast differences in intensity ranges which depend on the acquisition parameters. This is completed along with an expansion of the low intensities, for the HDR algorithm to function more effectively. The algorithm allows for the low intensities to be expanded whilst leaving the high intensities almost unchanged. This low intensity expansion is performed as HDR works more effectively on high intensity levels within an image.

The HDR companding algorithm is inspired by Dahari and Spitzer (1996) and Sakmann and Creutzfeldt (1969). This algorithm consists of two stages: the spatial building blocks and the adaption mechanism for gain control. The spatial building blocks are modeled as difference of Gaussians (DOG).

A resultant image can be seen in Figure 2.4. The algorithm successfully compressed and exposed the original HDR image into a singe low dynamic range (LDR) image. Statistically, the results were not inferior to diagnostics performed using the original HDR image but there were no statistically relevant improvements. The practical contribution of this work is the benefit of not requiring a professional mammography work station given the low dynamic range display of the resulting images.

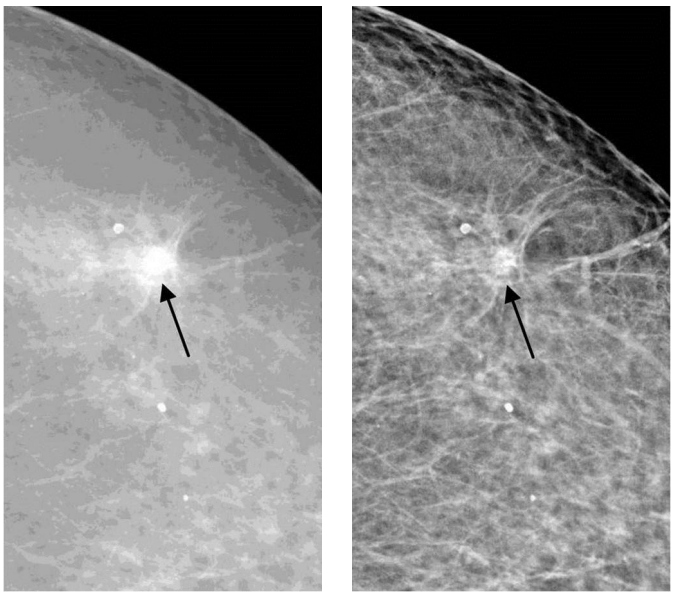

(a) Original Image. (b) BDMC Image.

Figure 2.4: Demonstration of mammography HDR algorithm (Kanelovitch et al., 2013).

2.5 Dual Exposure for Dynamic Range Extension

In X-ray diagnostics, it is common to have both low and high density regions within a single image. Yet the dynamic range of X-ray images is limited and compromises the diagnostic quality of the image. This is caused by a single X-ray image dynamic range not being large enough to hold the range required for such density differences. Consequently, the dense areas are obscured. An adjustment of the X-ray exposure for the dense regions subsequently causes the low density regions to be saturated. Sisniega et al. (2014) introduced a novel dual-exposure technique to extend the dynamic range of

flat panel detectors. The dynamic range of a radiograph was extended by the use of two acquisitions of a same sample but taken at different energy levels.

The first image was acquired with no pixel in the detector being saturated followed by an image that was partially saturated. The second scan aimed to provide more information on the denser regions that were not exposed in the first. The two scans were then combined using a maximum likelihood estimation, introduced by Robertson et al. (2003). To obtain this estimation, a basic pixel model was built assuming a linear relationship between exposure and pixel signal as well as the incoming photons following a compound Poisson model. To combine the two acquired datasets with the maximum likelihood estimate, a joint probability density function (j-PDF) was defined based on the pixel model.

The potential performance of the HDR method was evaluated by using simulated data with the pixel model. The actual performance was also evaluated for both planar and tomographic images with individual phantoms. Success in both the theoretical and experimental results showed that the dynamic range of an X-ray image can be extended using HDR methods. The dual exposure technique was able to provide valid signals for areas of high attenuation. The successful extension of the dynamic range using the HDR method allows for medical applications in regions with both low and high attenuations.

Several techniques applying HDR to medical imaging have been reviewed. None of these has been used in routine clinical applications, and none applying HDR to the visualisation of the C7/T1 junction have been reported in the literature.

2.6 Discussion

Despite the advances in HDR imaging, its application within the medical field is limited. The OCT dynamic range extension adopted a technique inspired by HDR but the virtual images and histogram distribution did not effectively represent a true extension of the dynamic range (Ishikawa et al., 2013). Using a single image and segmenting it into various images and further stretching the histogram created flaws, possible irregularities or unreliable information i.e. information that was not in the original image. The subsequent HDR and tone mapped image contained the risk of having false information created by the histogram distribution technique.

The simple application of the HDR technique by Trpovski et al. (2013) for dental radiographs and the results achieved show that HDR has a potential role in medical imaging. The maximum and minimum energy images considered the worst case images obtained and still allowed for a diagnosable image to be produced. A generalised approach was presented to obtain the equivalent exposure values for a radiograph which is vital for the HDR process. However, the approach does not consider images that are not at maximum and minimum energies. HDR is designed to maximise luminance channels and the effects of images between the extreme ranges need to be experimented with. Furthermore, the technique requires multiple scans, increasing the radiation exposure, and no clinical evaluation of the images was performed, thus the algorithm's effectiveness cannot be fully assessed.

An approach to reduce costs but improve image quality in the hip X-ray implementation shows promise but lacks feasibility (Florea et al., 2007). The introduction of photographic images of a radiograph to increase the dynamic range yields improved results but also increases the number of image acquisition techniques. However, the technique combined with its confidence value, did allow for better exposure value assignment. The image fusion techniques tested are not the classical HDR techniques but successfully produce images with increased number of brightness levels, effectively reproducing the HDR tone map effect.

The exhaustive approach taken to create the BDMC algorithm for mammography produced images that are detailed, sharp and exposed details hidden with the dynamic range of a mammogram (Kanelovitch et al., 2013). The contribution of the BDMC algorithm is the availability of the information in a single LDR image. This could allow for emergency, operating rooms or clinics to utilise all the available information in a mammogram without the radiographic viewing equipment on site and thus improving efficiency and lowering costs.

The dual exposure approach attempts to extend the dynamic range of X-ray images by the means of two differently exposed radiographs (Sisniega et al., 2014). The varied attenuation values throughout the resultant image found in the Sisniega et al. study shows that the HDR technique adopted is capable of revealing details of both low and high attenuation regions. The research was not applied clinically but the results suggest that regions of the anatomy that show a sudden change in attenuation would greatly benefit from the imaging technique.

Chapter 3

Methodology

This chapter describes the acquisition and processing of lateral radiographs of a C7/T1 junction phantom into an HDR image. Digital X-ray images already have a high dynamic range but are often limited to a low dynamic range display. HDR imaging techniques are applied in this chapter with the aim of improving the visualisation of the junction by increasing the visible range of an X-ray image. The technique is applied to both single and dual energy X-ray images. These are further processed with a region of interest analysis. A phantom was designed and constructed, of which images were acquired for testing of the HDR techniques.

3.1 Image acquisition and processing tools

The images for this project are taken on the Lodox Statscan, a system that uses linear slot scanning radiography (LSSR). This technique differs to conventional X-ray imaging in that instead of a conical beam of X-ray energy, the beam is shaped into a fan (Evangelopoulos et al., 2011). The difference is illustrated in Figure 3.1. This shaping effectively limits poor quality and scattered photons in the X-ray beam used for imaging. The image is acquired using line scanning - an image built up by taking successive rows of data. LSSR also has an intensity decrease that is directly proportional to the distance as compared to the conventional inverse square law (Potgieter et al., 2005). All the above allows for a much smaller dosage exposure, which is the major advantage of the Lodox System. However, this method does not reduce the disadvantage that exists for the C7/T1 junction.

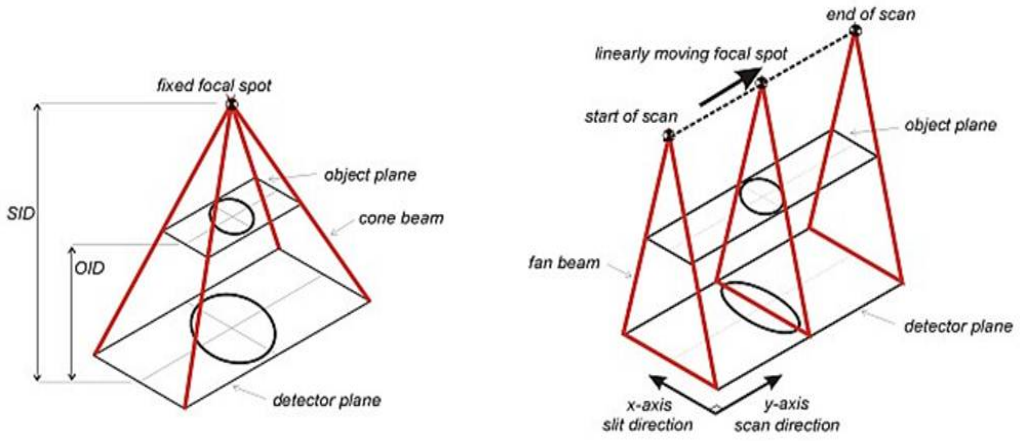

(a) Cone-beam geometry (b) Slot scanning geometry

Figure 3.1: Difference between conventional and linear slot scanning radiography, adapted from Potgieter et al. (2005).

The Lodox Statscan offers a range of scanning energies depending on the anatomical region and size of the patient. The Statscan also has a C-arm that is able to rotate and take images from different orientations. Scans that require the C-arm with the X-ray source rotated into the lateral scan position (90^o) include the cervical; thoracic and lumbar; and the full lateral. The scan types and corresponding energy levels can be seen in table 3.1. The current for each energy and patient size vary from 125 mA for 80 kV; 160 mA for 90 kV and 200 mA for the remainder. Included with the Lodox Statscan is a proprietary automatic image optimisation method known as 'Lucid'. This method facilitates edge enhancement and histogram equilisation (Pitcher et al., 2008)

Table 3.1: Lodox statscan scan type and energy level.

	Energy Levels			
Scan type	**Small (kV)**	**Medium (kV)**	**Large (kV)**	**X-Large (kV)**
C- Spine	80	90	100	110
TL Spine	100	120	130	140
Full lateral	130	135	140	145

The X-ray images were processed and analysed using MatLab and the HDR functions available in the MatLab image processing toolbox. The radiance information extraction, tone-mapping and reconstruction algorithms for HDR imaging rely on matrix operations and this implementation is facilitated in MatLab (Webb, 2008). The *"HDR Toolbox for MatLab v1.0.5"*, created by Banterle et al. (2011), contains a wide variety of tone mapping algorithms. It is compatible with the built in MatLab HDR functions and is used in conjunction to further process the obtained images. The toolbox is distributed under the GPL v3 license. The processing was done on an Intel Core i5 - 310M, 2.5 GHz laptop with 8 Gb RAM running Windows 7 Premium.

3.2 Phantom Design

The phantom was constructed with polymethyl methacrylate (Perspex) containers, a body of water, human cervical and thoracic vertebral dry bones and shoulder girdle dry bones (clavicle, scapula and humerus). The bones were obtained from the Department of Human Biology of the University of Cape Town from cadavers donated for research purposes.

Perspex and water were selected due to their relative attenuation coefficients being similar to that of soft tissue and skeletal muscle as seen in Figure 3.2. Cervical and thoracic vertebral bones were used to construct the C7/T1 junction, whilst the shoulder girdle bones (including the humerus) created the obstruction (refer to Figure 2.1). Three containers were made from 4 *mm* thick perspex - two holding the shoulder girdle and one holding the vertebral bones. The containers are separate and allows for individual imaging of each set of bones. The individual imaging was for testing and evaluation purposes to see the effects of the HDR algorithm on the full junction and the cervical vertebrae alone.

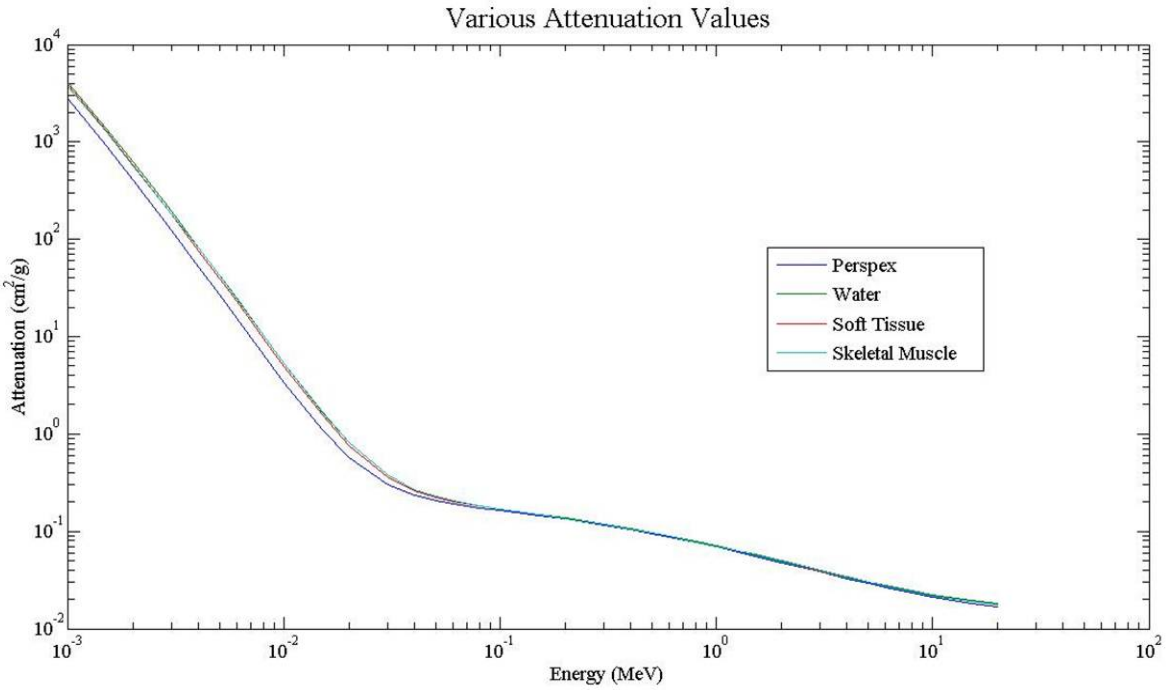

Figure 3.2: Water, perspex, soft tissue and skeletal muscle attenuation across photon energies.

The dimensions and design of the box can be seen in Figures 3.3(a) & 3.3(b). The dimensions were set to fit a large shoulder girdle to maximise the obstruction, that is to recreate the C7/T1 junction of a large patient. In order to minimise the compounding

effects of a thick layer of Perspex, the top Perspex sheet was angled at 30^o. The angle and sheet thickness creates a 10 mm thick layer of perspex for the X-rays to penetrate (See Figure 3.4). This thickness along with the body of water creates an attenuation similar to that of human soft tissue. It should be noted that only the left shoulder container design has been shown. The right shoulder has the identical dimension but in the mirror image. The bones are connected with Pratley Quickset Whiteglue. The adhesive strength, low cost, ease of application and low attenuation during X-ray imaging make it suitable for this application. The thickness of the Perspex sheets were chosen in order to minimise the attenuation but still contain the large body of water and bones without breaking.

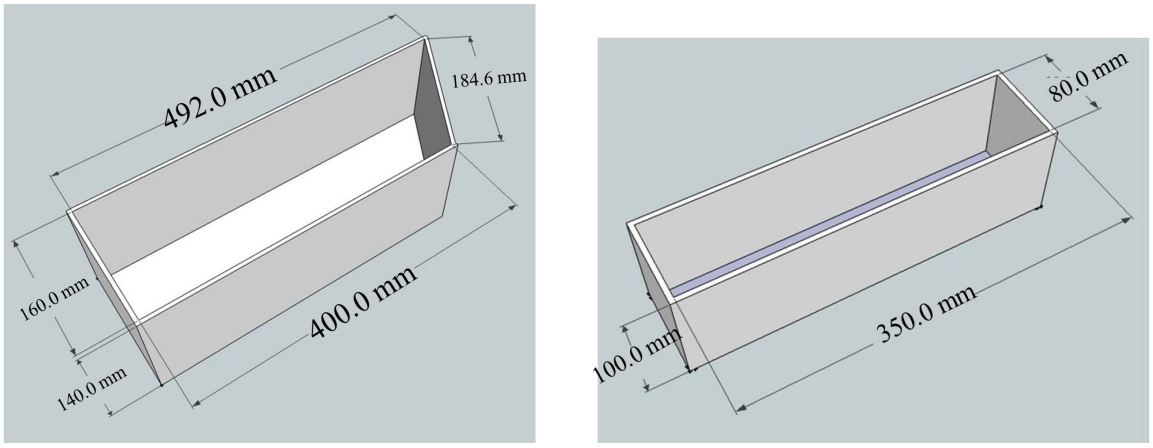

(a) Shoulder girdle container dimensions. (b) Vertebrae container dimensions.

Figure 3.3: Phantom containers and their respective dimensions.

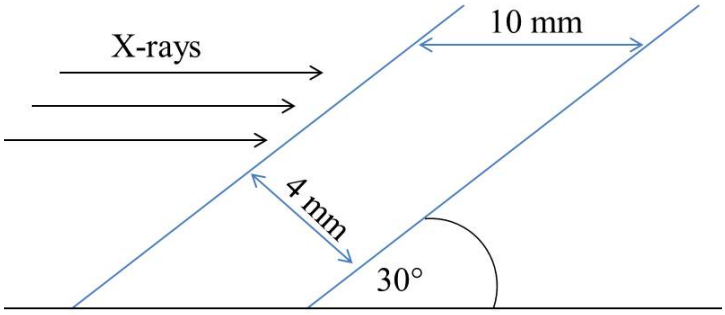

Figure 3.4: Thickness of the top Perspex sheet which the X-ray energy penetrates (top view).

3.2.1 Shoulder Girdle Phantom

The constructed phantom with the shoulder girdle bones can be seen in Figure 3.5. The phantom successfully holds all the pre-arranged bones. It is able to fit entirely onto the Lodox scanning trolley.

Figure 3.5: Phantom with bones placed.

3.3 Single Image HDR

This section explains the application of the HDR imaging techinque to single X-ray images. The single X-ray HDR methodology is based on the technique described in §2.3 and the available functions in the MatLab HDR toolbox. The multiple exposure principle is reproduced within a single X-ray image by viewing the HDR radiograph within certain contrast windows. These contrast windows act similarly to differently exposed photographs - revealing different lighting / X-ray contrasts within the image. The individual images created by these windows were merged using the HDR image acquisition technique described below. The individual images are combined using tone mapping algorithms described in §2.3.1.

3.3.1 Individual image acquisition and HDR processing

Lateral radiographs obtained from the Lodox Statscan are in the DICOM[1] (DICOM, 2014) format to retain the information stored in its dynamic range. Each X-ray image was preprocessed into separate images with various contrast (or display) window sizes. The window size is either set or varied with the number of images being used in the HDR, depending on the processing technique.

The set window size is half of the entire contrast range - an example of the initial window and the window across the middle of the contrast range is shown in Figure 3.6. This window shifts through the contrast range and obtains a number of images depending on the number of images used to create the HDR image. This technique involves a large amount of repeated/redundant information but prevents small contrast windows containing little to no information when the number of images increases.

The second technique uses a varying window size through the contrast range to develop the HDR image. This is illustrated in Figure 3.7 for one instance of a window size. This window size is changed depending on the number of images selected and ranges across the entire contrast window as illustrated. This removes the redundant information but involves smaller contrast windows when the number of images used in the HDR construction increases. Each approach (set or varied window size) is applied to single X-ray images.

[1]Digital Imaging and Communications in Medicine

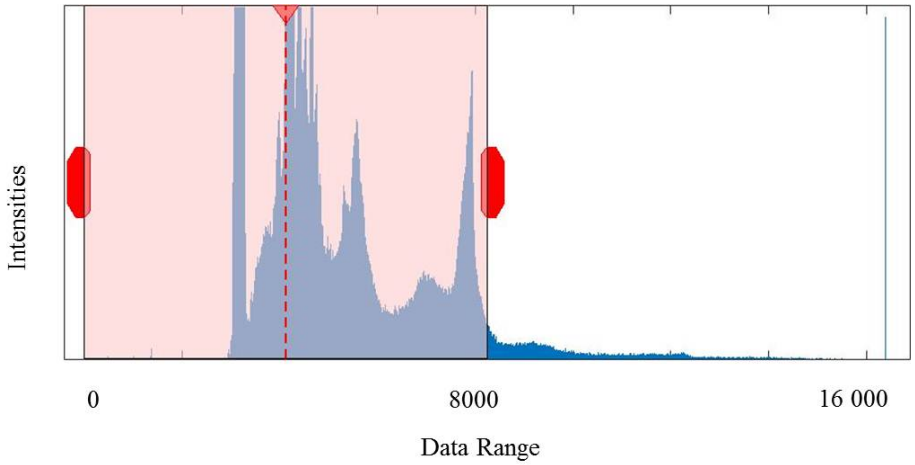

(a) Half contrast window at initial data range.

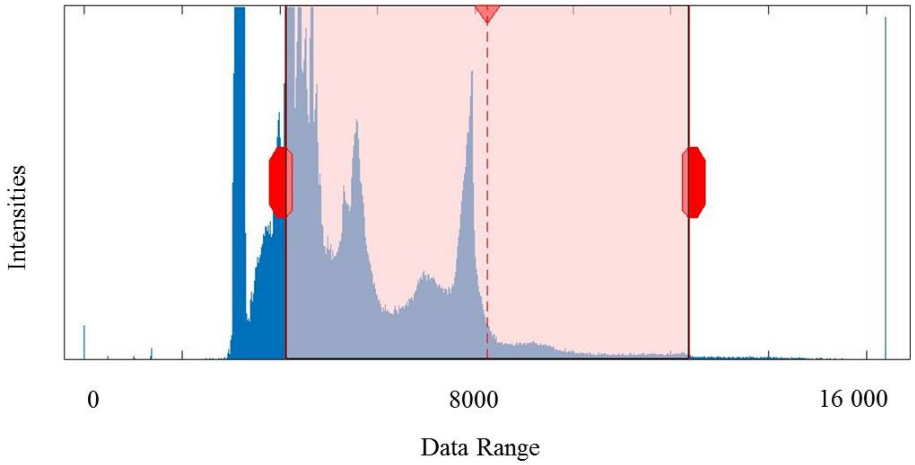

(b) Half contrast window at central data range.

Figure 3.6: Contrast window range at half the entire contrast data range at the initial and central data ranges.

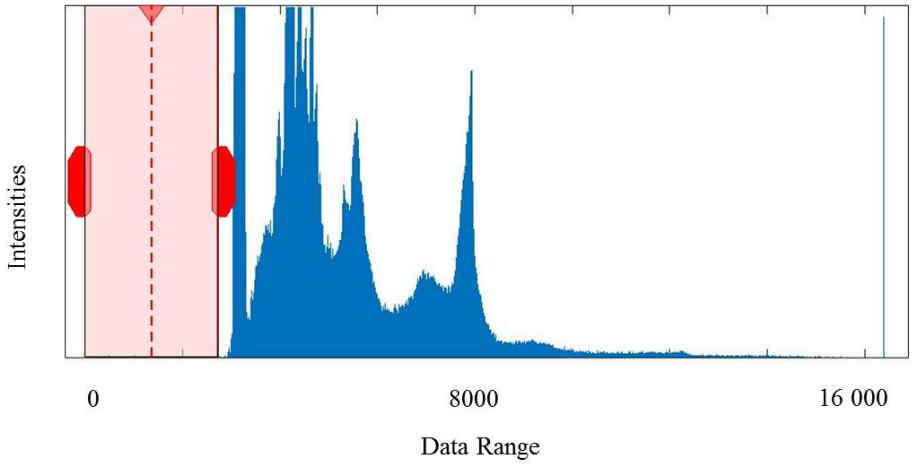

(a) Varied contrast window at initial data range.

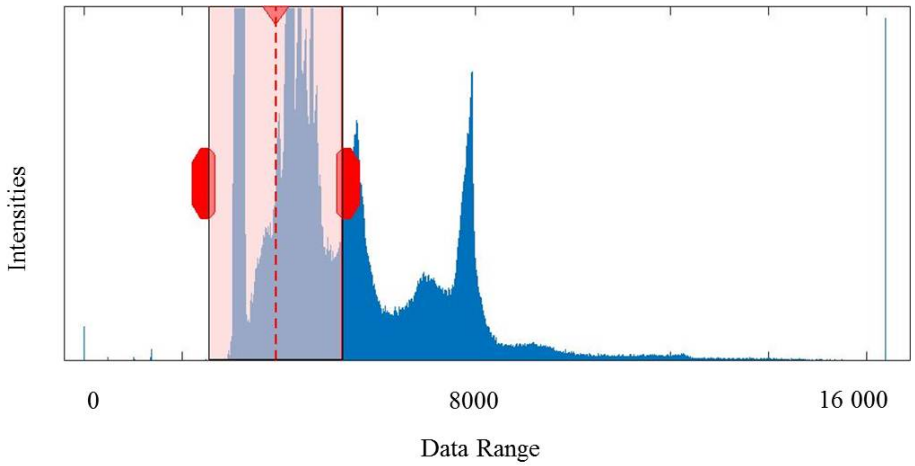

(b) Varied contrast window at second data range.

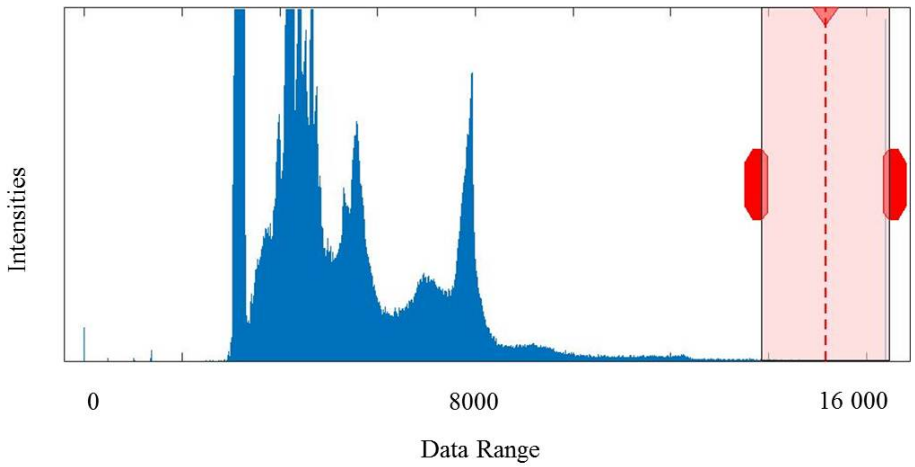

(c) Varied contrast window at final data range.

Figure 3.7: Contrast window range of varying size with no overlap.

The separate window images effectively reproduce the multiple exposure technique used in HDR photography. The image with the "optimal" exposure value (EV = 0) is created with a window size of half the entire contrast range and centrally located (Prakel, 2009). This is shown graphically in Figure 3.6(b). This window size and position is chosen because it corresponds to a correctly exposed photograph i.e. maximised visibility of all aspects in the image. The subsequent images are created by shifting the contrast window (with the fixed or varied size) across the entire contrast range.

A single X-ray image has a dynamic range that contains information at both contrast extremes that hold little to no useful information. An example for the varied contrast window size can be seen in Figure 3.8 where Figure 3.8(a) and Figure 3.8(b) are images at each contrast extreme. The figures hold no beneficial information when included in the algorithm for the C7/T1 junction and are removed.

The contrast display window is limited to a region where useful information is contained by scaling the display range by applying a MatLab built in correction factor. This correction eliminates 2% of the outlying contrast ranges and thus eliminates the upper and lower extremes to reduce the display range to contain useful information held by the image.

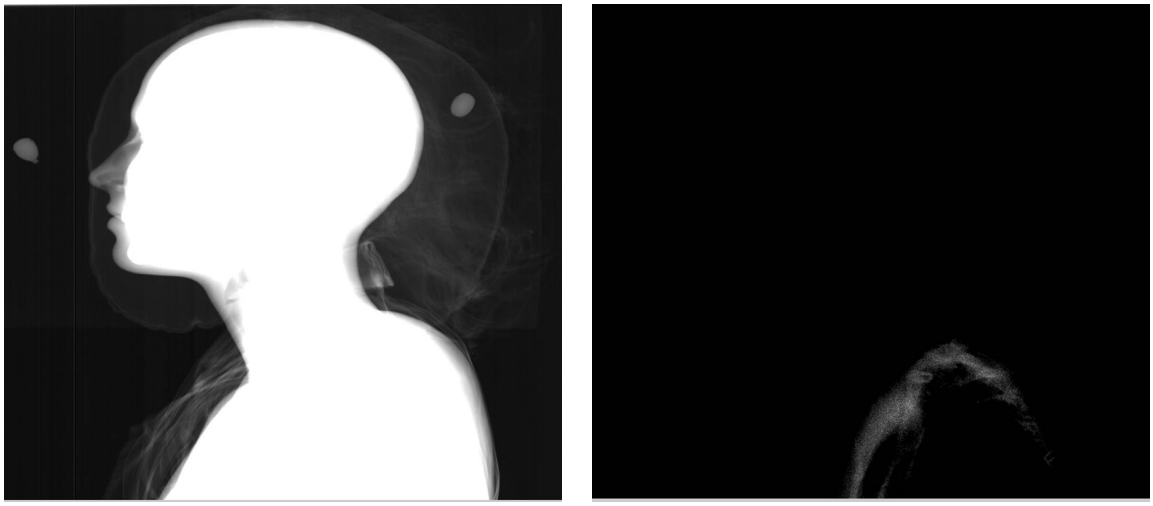

(a) Contrast window at lower extreme. (b) Contrast window at upper extreme.

Figure 3.8: X-ray images at the contrast extremes.

The preprocessing described above uses the DICOM file to separate the images into its individual contrast windows. The images are then stored in a Joint Photographic Experts Group (JPEG) format. JPEG is a compressed file that reduces both the file size and quality - quality dependent on the extent of size reduction. MatLab provides a lossless compression. JPEG is also used as it is an RGB image − necessary for the MatLab HDR algorithm.

3.3.2 Exposure Value Estimation

In order to construct the HDR image, MatLab requires either an exposure value (EV) or a relative exposure (RE) for each image. The exposure value is a system developed to link the film speed/digital sensitivity, lens openings (aperture) and shutter speeds (Prakel, 2009). These values are typically integers. Some common values and their lighting environment can be seen in Table 3.2. These are typical values but may vary depending on the camera specifications. Relative exposure values are simply values within ratio to one another. That is, an image with RE of 1 will have double the exposure of an image with RE of 0.5.

Table 3.2: Common Exposure Values (Prakel, 2009)

Exposure Value	**Lighting**
5	Moonlit scene.
8	Bright night street scenes.
13	Partly cloudy but bright day.
18	Bright sunlight.

An X-ray image and a digital photograph do not have the same exposure value and their exposure times cannot be estimated by the same means. Considering that an HDR image is taken at a single lighting with different exposure values, the values can be broadly classified into:

- Underexposed - Negative EV (darker/dimmer image).
- Normally exposed - 0 EV (Ideal image).
- Overexposed - Positive EV (lighter/brighter image).

In this study, the exposure value for each image is estimated as negative for low contrast/darker images and positive for higher contrast/brighter images. These values are scaled according to their respective contrast window positions and the number of images used (the window images at lower and higher contrasts receive the larger magnitude EV). These values are then varied in order to obtain images with different exposure values for the same X-ray image. The various exposure value combinations and the images produced are visually evaluated to ensure the exposure value that has been allocated is suitable.

3.3.3 Tone mapping

Once the HDR image is constructed from the window images, tone mapping is performed to render it back into a suitable range for display. Five tone mapping algorithms are identified for processing of the HDR images. These are: MatLab standard built in algorithm; Lischincki; Normalise; Reinhard and Ward histogram adjustment tone mapping. The Lischinski, Reinhard; and Ward algorithms in §2.3.1 are implemented in the *"HDR toolbox for MatLab"*. The normalise algorithm is also implemented in the toolbox and is the luminance map normalized by the maximum luminance value.

The process of image acquisition and tone mapping for HDR image reconstruction is shown in Figure 3.9. The process begins with the Lodox scan. Once this is complete, the scan is split into multiple window images (as according to the contrast window methodology described above). A check is performed to see if the perscribed number of window images for all the multiple exposures has been constructed. Once this is complete, each image is assigned an EV. The HDR image is constructed using the built in MatLab toolbox and then tone mapped. A check is then performed to ensure that the various preset EV combination ranges have been completed. Once all of these EV combination ranges are complete, the processing for that single X-ray image is complete.

3.4 Dual Energy X-ray HDR

The multiple exposure technique in photography can be approximated by using multiple X-ray images taken at two different energy levels - dual energy images. Traditionally, these images are used for bone and soft tissue measurement and are obtained by passing two beams at different energies through a common body (Mazess et al., 1990; Svendsen et al., 1993). The beams experience different degrees of attenuation depending on the mass and type of tissue that they pass through.

In photography, the multiple exposure technique is used to obtain details from a scene that a single photo will not be able to. Details in both dark and bright regions within the same scene can be captured within a single image if the multiple exposure effectively increases the dynamic range. The dual energy X-ray imaging process mimics this technique by acquiring two scans at different energy levels - levels specified for different regions of the body. The HDR and tone mapping algorithms are then used to combine the images which are expected to have exposed different details of the lateral spine.

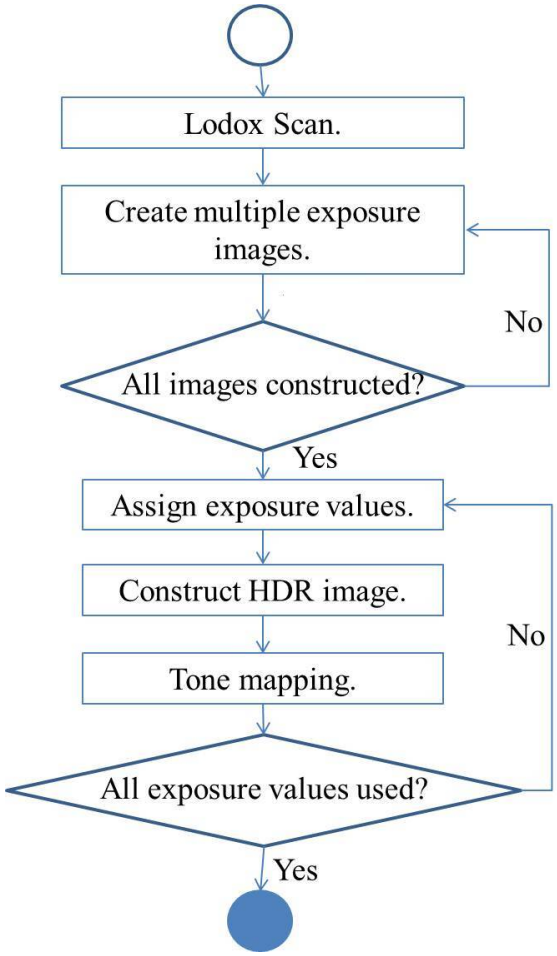

Figure 3.9: Flow chart of a single X-ray HDR image acquisition and tone mapping.

Direct control over the energy levels is available for the Lodox Statscan. 36 sets of dual energy images were obtained. The different energy combinations are presented in Table 3.3.

Table 3.3: Exposure value ranges for dual energy scans.

	90 kV	**100 kV**	**110 kV**	**120 kV**	**130 kV**	**135 kV**	**140 kV**	**145 kV**
80 kV	✓	✓	✓	✓	✓	✓	✓	✓
90 kV		✓	✓	✓	✓	✓	✓	✓
100 kV			✓	✓	✓	✓	✓	✓
110 kV				✓	✓	✓	✓	✓
120 kV					✓	✓	✓	✓
130 kV						✓	✓	✓
135 kV							✓	✓
140 kV								✓

To retain the information obtained by the dual energy scans, the number of images used to construct the HDR image was doubled. If a single X-ray HDR image contained 3 images at various exposures, a dual energy scan will have 6. This maintains consistency

across the analysis techniques. The exposure value assignment was identical to that of the single X-ray algorithm for each image at its energy level.

Each of the constructed dual energy scans was varied by presence/absence of the Lucid image enhancement described in §3.1, the number of images, and the contrast window sizes (these variations are applied for each combination in Table 3.3). Each image was processed with the different exposure values to create a unique HDR image with a corresponding tone mapped LDR image. The images constructed can be seen graphically in Figure 3.10.

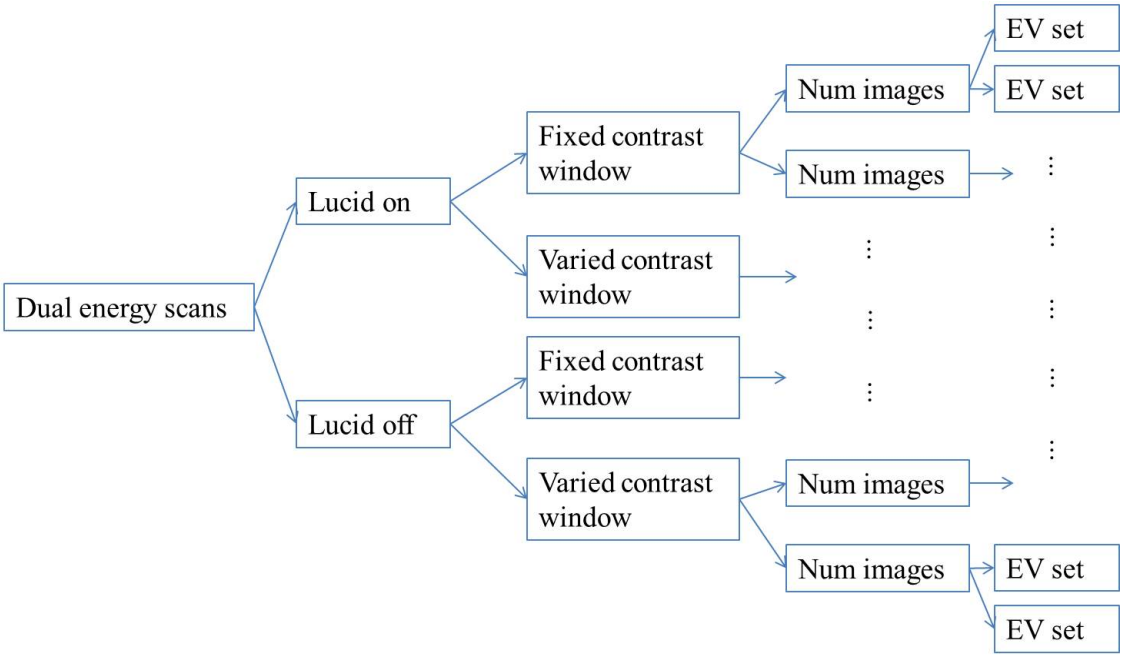

Figure 3.10: Breakdown of number of constructed images per dual energy scan.

The investigations undertaken can be summarised into the single and dual energy approaches. These approaches will use the phantom with and without water in order to analyse the final tone mapped images. The tone mapped images are produced using an HDR image created from window images using both the fixed and variable window sizes.

3.5 Region of Interest Analysis

The dual energy HDR method was combined with a region of interest (ROI) analysis. This was aimed at improving the C7/T1 junction. MatLab provides extensive region of interest analysis functionality and was used to process both single and dual energy scans.

ROI analysis is initiated with the user selecting the cervical region of the vertebrae. MatLab functionality allows the user to mark out a polygon of the desired region. The lowest co-ordinate of this polygon is taken as the cutoff point of the cervical region and the image is segmented into two at this point. An example of this process can be seen in Figure 3.11. In this example, the bottom left point will be used as the cutoff point for the cervical region. The remaining part of the image is assigned as the thoracic region. The variable HDR processes, EV's and tone mapping algorithms are expected to have different effects on these separate regions.

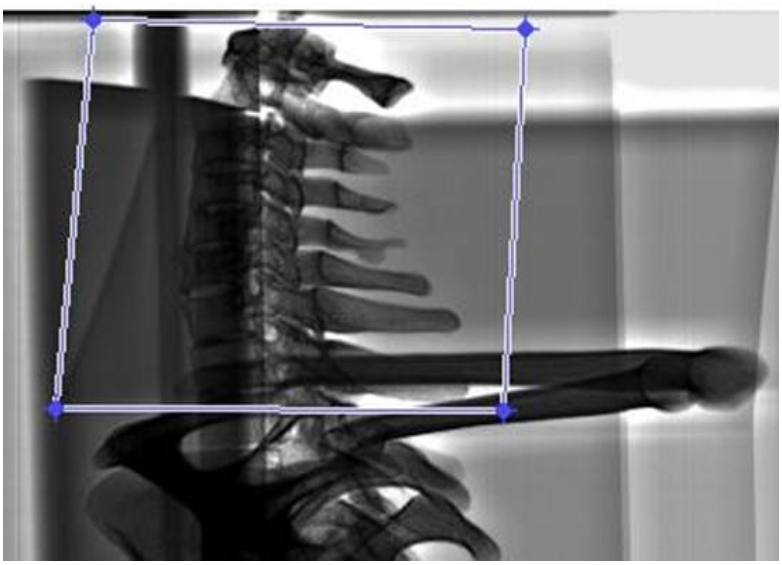

Figure 3.11: Region of interest analysis selection of cervical region.

X-ray radiation attenuates depending on the material and thickness of the object that it is penetrating. Because of this characteristic and the difference in anatomical structure between the cervical and thoracic regions, the HDR image for these regions use different dual energy combinations. The higher kV dual energy combinations are used to develop the thoracic HDR image, whilst the lower energy combinations are used to produce the cervical HDR image.

ROI analysis was done to explore the effect of separate HDR processing on the cervical and thoracic regions. The ROI locations for the cervical and thoracic spine images (i.e. the separation between the cervical and thoracic parts of an image) were determined by trial and error, by visually assessing the results of applying HDR processing on different ROI selections.

3.5.1 Image Evaluation and Signal to Noise Analysis

The resulting HDR tone mapped images are initially subjected to a qualitative evaluation based on the clarity and visibility of the C7/T1 junction. Each image is isolated and viewed independently for overall image usability. The images are then evaluated in conjunction with:

- Various EV combinations
- Tone mapping algorithms
- Energy combinations (dual and ROI analysis)

A qualitative analysis is performed preceding the signal to noise ratio so that only relevant images are processed further for a quantitative result.

The image quality of the radiographs produced using the ROI HDR analysis was assessed using the signal to noise ratio (SNR). The SNR is a quantitative way of expressing how noise compares to a signal (Bushberg et al., 2002). Considering an image signal "S" as a contrast "C" and intensity "I", the following equation arises as explained by Bushberg et al.:

$$S = C \times I \tag{3.1}$$

The SNR is defined as:

$$SNR = \frac{S}{\sigma} \tag{3.2}$$

where σ is defined as the noise in the signal. Taking note that the background intensity is the number of photons passing through "N", Equation 3.1 becomes:

$$S = C \times N \tag{3.3}$$

With this equation and that $\sigma = \sqrt{N}$, the following SNR equation arises:

$$SNR = C \times \sqrt{N} \tag{3.4}$$

This implies an increase in SNR with an increase in photons (Bushberg et al., 2002). This ratio is calculated using the "*snr*" function in MatLab. The function returns the SNR by computing the ratio of a signal' Fs summed square magnitude to that of the noise. The result is presented in decibels. Reference images of the cervical and thoracic vertebrae were required in order to calculate the SNR. These were taken at the varying

energy levels and without the shoulder girdle portion of the phantom. This was to create the ideal image of the C7/T1 junction without the obstruction of the shoulder girdle, against which to compare different output images.

The SNR measure provides a quantitative way to compare the HDR tone mapped image with a reference image and assess quantitatively the effect of HDR processing.

Chapter 4

Results

The results of the single image HDR, the dual energy HDR, the region of interest and the SNR studies are given in this chapter. The results of the single X-ray image approach are shown first as the initial approach to attempt to extract as much information from a single scan as possible. In practice, this would minimise the radiation exposure to the patient.

This is followed by the results of the dual energy approach to further extend the range of energy levels used within each radiograph, and thus extending the amount of information to be extracted. Finally, the results of the region of interest analysis, done in order to isolate the cervical and thoracic regions, are shown along with the relevant SNR results.

The phantom was tested with and without water to examine the effects of attenuation. The tests initially used 3 images at 3 different dynamic ranges. This was then increased to 5 images and dynamic ranges. The images were combined using different tone-mapping algorithms and the results were compared.

4.1 Single Image HDR Results

The single image HDR algorithm was tested by obtaining each scan listed in Table 3.1, divided into the window images, combined into an HDR image and tone mapped. This table lists all the different energy levels used for each category being scanned. HDR images were constructed from both 3 and 5 images of the phantom with no water. Both fixed and varying window sizes were tested for each image and images were tested with and without application of the built-in Lodox Lucid mapping. The figures shown in the

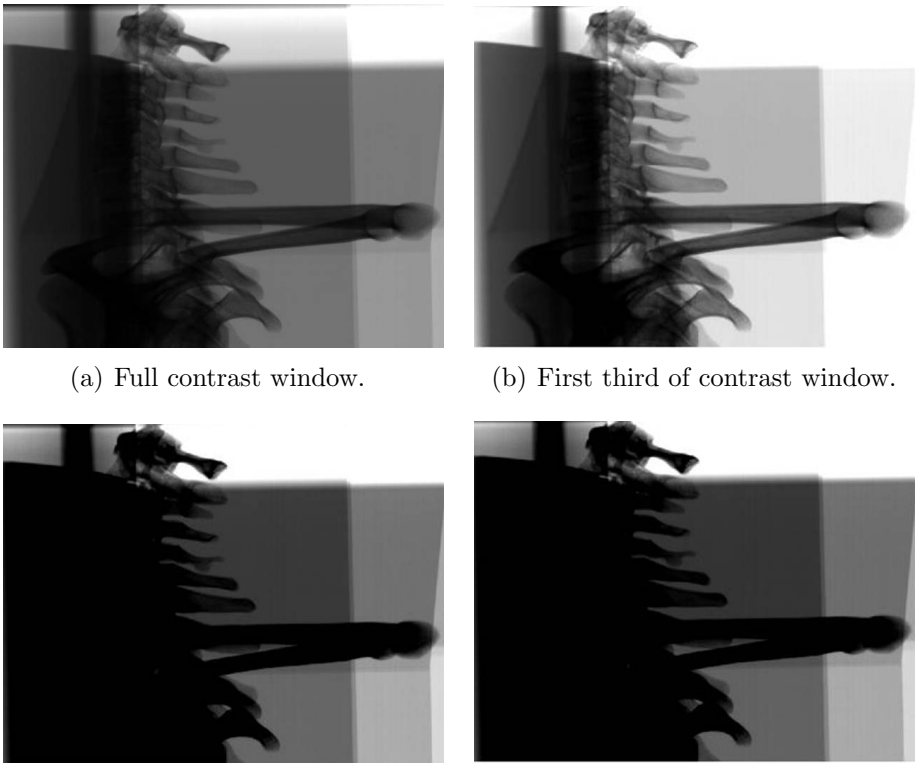

(a) Full contrast window. (b) First third of contrast window.

(c) Central contrast window (EV = 0). (d) Last third of contrast window.

Figure 4.1: Orignal 80 kV C-spine scan without Lucid split into 3 window images with the same size contrast window.

following results are a representative set of images to display typical results.

The exposure values for the tone mapping algorithms were varied as seen in Table 4.1 depending on the number of images. The initial and final exposure values (-8 & 8) were increased in steps of 2. The original scan without Lucid and showing the entire, initial, middle and final third of the contrast window can be seen in Figure 4.1. These windows are the first third of the entire contrast window, the middle third (central value being the central contrast as seen in Figure 3.6(b)) and the final third of the data range.

Table 4.1: Exposure value ranges for number of images.

3 images EV Range	**5 images EV Range**
-8; 0; 8	-16; -8; 0; 8; 16
-6; 0; 6	-12; -6; 0; 6; 12
-4; 0; 4	-8; -4; 0; 4; 8
0; 0; 0	0; 0; 0; 0; 0
4; 0; -4	8; 4; 0; -4; -8
6; 0; -6	12; 6; 0; -6; -12
8; 0; -8	16; 8; 0; -8; -16

4.1.1 Three-Image Windowing

A typical result can be seen in Figure 4.2, which shows a 80 kV lateral C-spine scan after the HDR and tone mapping. This scan is of the phantom not containing water, 3 images combined using the built in MatLab tone mapping algorithm, a fixed size contrast window and Lucid applied. This image is produced and shown first as it is the simplest implementation of the HDR and tone mapping process within MatLab. The exposure values listed are those of the three images used to create the final HDR tone mapped image. From these images, it can be seen that the estimation for negative EV's described in §3.3.1 for darker images is appropriate i.e. images with a darker contrast receive a negative EV whilst brighter images receive a positive EV. Such estimation then produces an image that is visually more appealing and informative than the EV estimation counterpart i.e. where darker contrast images were assigned a postive EV (Figure 4.2(a) vs. Figure 4.2(c)).

4.1.1.1 Varying Tone Mapping Algorithms

The Lischinski, Normalize, Reinhard and Ward histogram adjustment tone mapping algorithms were tested. The images can be seen in Figure 4.3. The differences are subtle and image appearances vary depending on the exposure value in the HDR image. The exposure values $-4; 0; 4$ produce darker images throughout all algorithms, despite having the clearest image with the built-in MatLab tone mapping algorithm (Figure 4.2(a)). This algorithm highlights the bone from the background. These images do not provide any subjective improvement on the visualisation of the C7/T1 junction using the built-in MatLab tone mapping algorithm (as seen in Figure 4.2(a)). Considering that the phantom did not contain water, thus significantly lowering the attenuation at the junction, the produced images do not provide any improvement on the visibility of the junction.

4.1.2 Five-Image Windowing

The 80 kV C-spine scan without Lucid tone mapping, 5 window images and varying contrast window sizes for HDR construction, can be seen in Figure 4.4. These images use the built-in MatLab tone map algorithm. The images exhibit similar traits to that shown in Figure 4.2 where negative EV estimates for darker images result in a visibly more informative composite image.

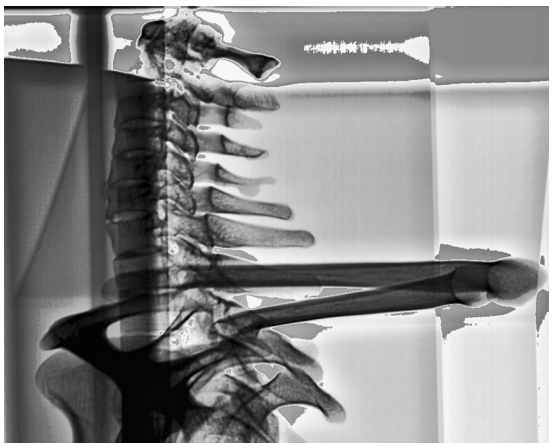

(a) EV: -4; 0; 4.

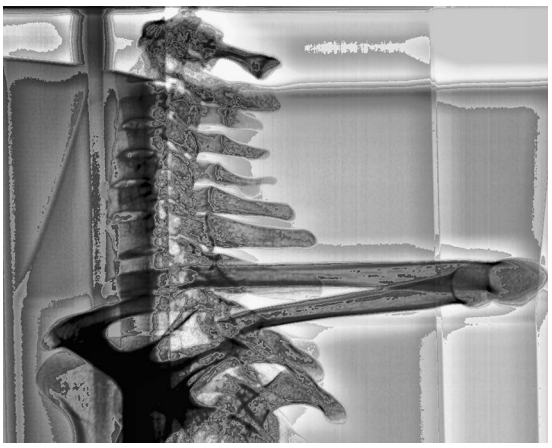

(b) EV: 0; 0; 0.

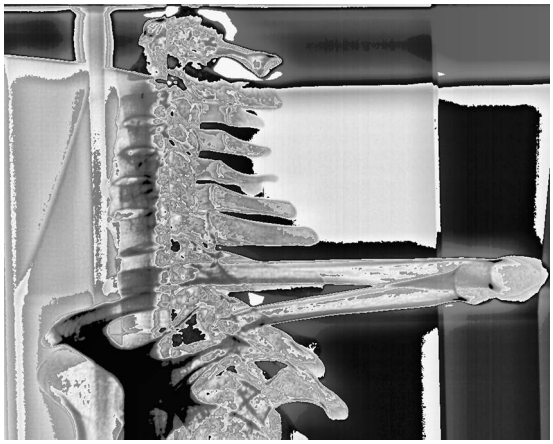

(c) EV: 4; 0; -4.

Figure 4.2: Tone mapped image results of single 80 kV C-spine Lucid scan with 3 window images with fixed contrast window for HDR processing using built in MatLab tone mapping.

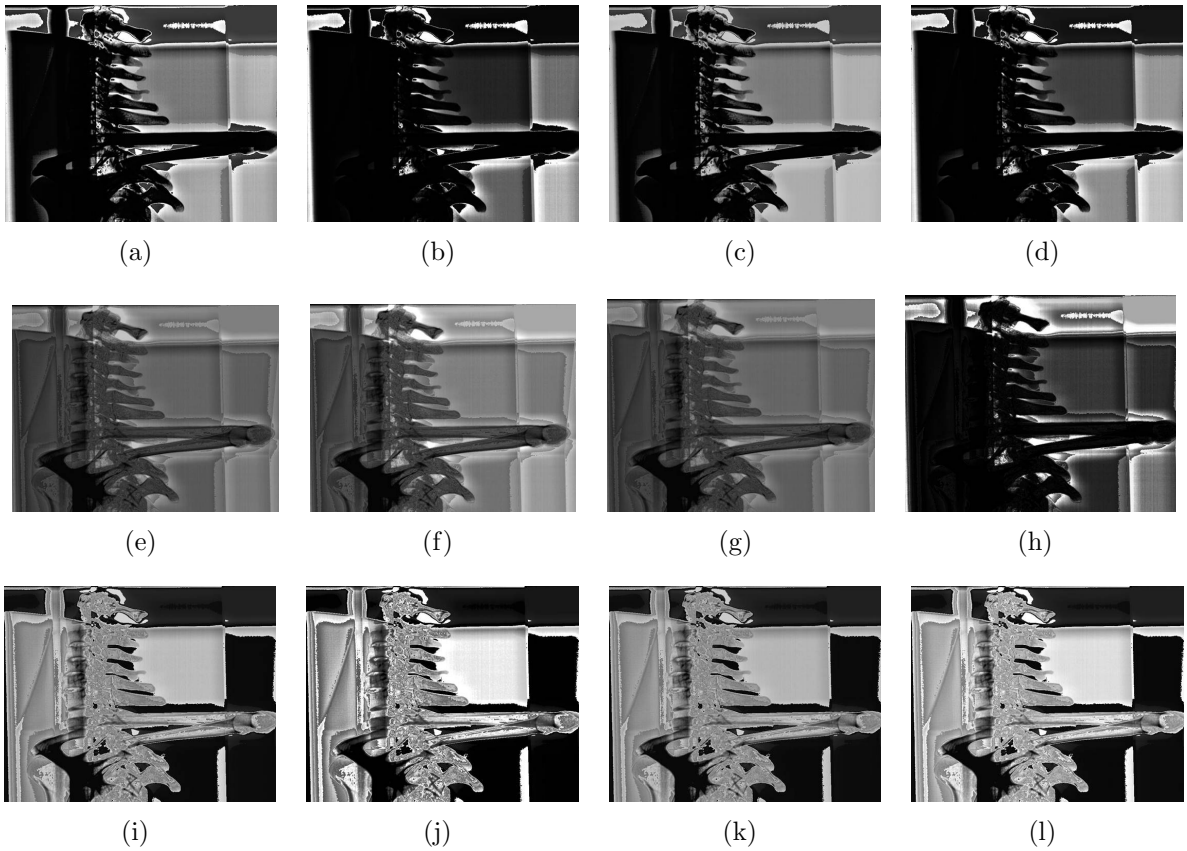

Figure 4.3: Tone mapped results of single 80 kV C-spine scan with Lucid, 3 window images for HDR processing using the Lischinski ($a,\ e,\ i$), Normalize ($b,\ f,\ j$), Reinhard ($c,\ g,\ k$), and Ward histogram adjustment ($d,\ h,\ j$) tone mapping. Images $a - d$ use EV's -4; 0; 4; $e - h$ use EV's: 0; 0; 0 and $i - l$ use EV's: 4; 0 ;-4.

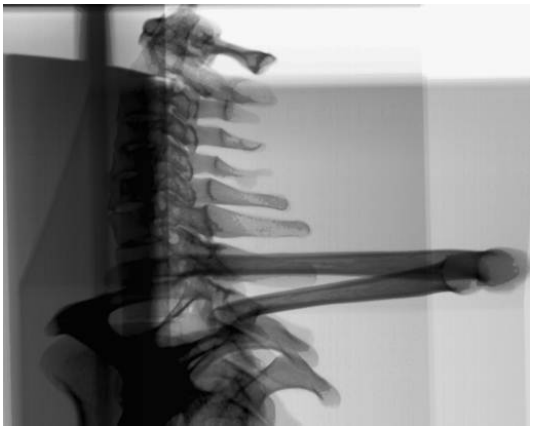

(a) EV: -4; -2; 0; 2; 4.

(b) EV: 0; 0; 0; 0; 0.

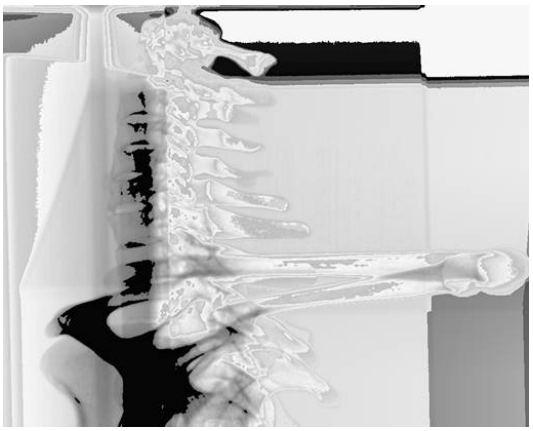

(c) EV: 4; 2; 0; -2; -4.

Figure 4.4: Single 80 kV C-spine no Lucid scan with 5 window images with varying contrast window for HDR processing using built in MatLab tone mapping.

4.1.2.1 Varying Tone Mapping Algorithms

The same set of images are also tone mapped with the Lischinski, Normalize, Reihnhard and Ward histogram adjustment tone mapping algorithms and the results can be seen in Figure 4.5. The similarity between this figure and Figure 4.3 is clear. The trend is consistent showing that the exposure values have similar effects. EV's (-4; 0; 4) produce darker images whereas EV's (0; 0; 0) create an image between that of EV (-4; 0; 4) and EV (4; 0; -4).

The 5 window image tone mapped images are darker than the 3 window image tine mapped images in Figure 4.3. This is because the contrast window sizes are made smaller in order to fit the increased number of images into the entire dynamic range. This smaller contrast window limits the upper and lower intensity levels. For images with contrast windows in the lower contrast ranges, the resultant image is darker. The same for images in the higher contrast ranges and brighter images. This occurs despite the contrast correction factor described in §3.3 being applied. The overall HDR image is darker because HDR attempts to highlight the luminance of an image, thus the values at the extremes are favoured. The darker (black) pixel values are favoured in comparison to the less intense gray values. Furthermore, the correction factor removes the intense (brighter) white values and focuses the the contrast range more on the darker contrast ranges so as to highlight the grayscale nature of X-ray images. The increase in the number of images acquired in an X-ray HDR process using a single scan with a varying contrast window size does not improve the C7/T1 visibility and in some tone mapping cases, worsens it.

4.1.3 Varying Energy Levels

Figures 4.2 to 4.5 are at 80 kV and 125 mA, of the phantom containing no water. Figure 4.6 shows how the image changes at different energy levels. Comparing Figure 4.6(a) to Figure 4.6(f) it can be seen that, as expected, with an increase in kV and mA, the cervical vertebrae fade whilst the penetration in the thoracic junction region is increased. The figure shows energy levels up to 120 kV as after this value, the X-ray penetration is too great and effectively clears the vertebrae and reveals parts of the far shoulder girdle. This occurs due to the lower attenuation of the phantom without water.

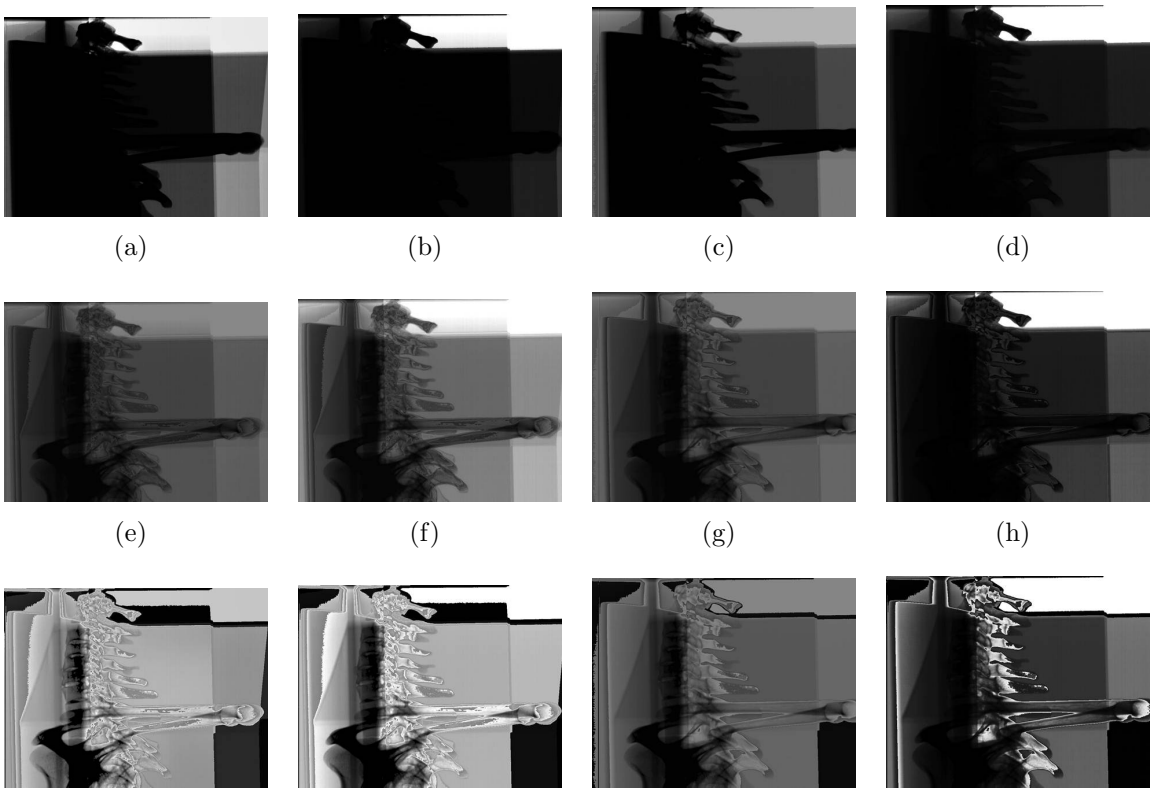

Figure 4.5: Single 80 kV C-spine scan with no Lucid, 5 window images for HDR processing using the Lischinski $(a,\ e,\ i)$, Normalize $(b,\ f,\ j)$, Reinhard $(c,\ g,\ k)$, and Ward histogram adjustment $(d,\ h,\ j)$ tone mapping. Images $a-d$ use EV's -4; -2; 0; 2; 4; $e-h$ use EV's: 0; 0; 0; 0; 0 and $i-l$ use EV's: 4; 2; 0 ; -2; -4.

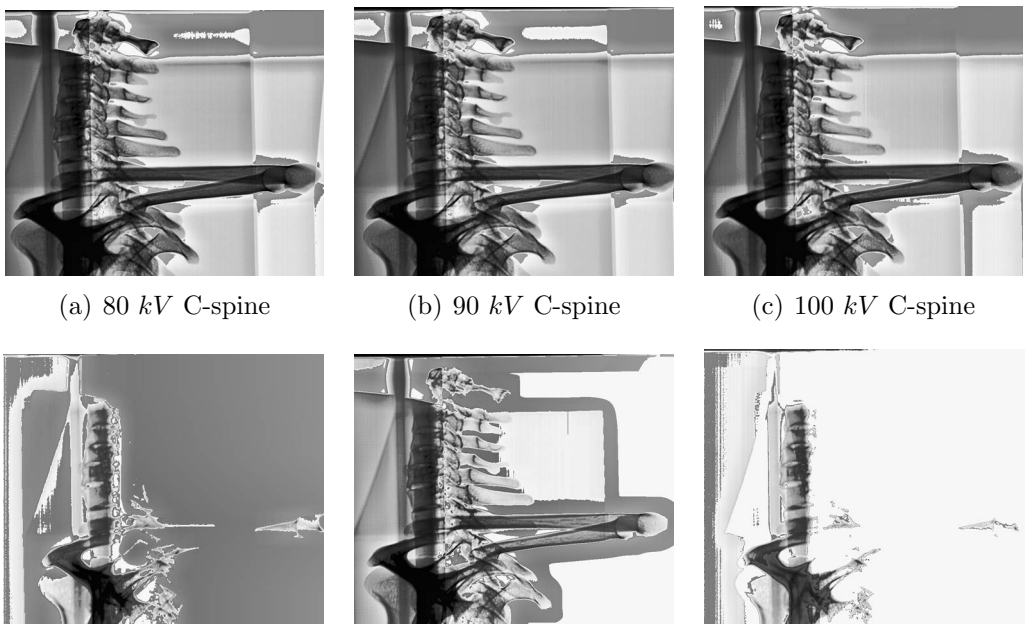

(a) 80 kV C-spine (b) 90 kV C-spine (c) 100 kV C-spine

(d) 110 kV C-spine (e) 100 kV TL-spine (f) 120 kV TL-spine

Figure 4.6: Various scans at preset Lodox energy levels for various cerivical and thoracic-lumbar vertebrae with 3 image, fixed contrast window, -4;0;4 exposure values, Lucid and the built in MatLab tone mapping algorithm.

4.1.4 Discussion

A single X-ray scan of the constructed phantom without water provides an image with the humerus, scapula, clavicle and perspex obstructions of the C7/T1 junction. This scan gives a false sense of the detail that is acquired from an actual lateral scan due to the difference in attenuation between the soft tissue in a real patient and the lower attenuation in the shoulder phantom with no water. However, the scans provide a means to analyse the effects of the HDR and tone mapping algorithms on an X-ray image. The bands that are present in the scans are due to the height of the Perspex container not being able to cover the entire bone structure within it - the clavicle sits outside/above the phantom container. The changes in the perspex attenuation cause the various contrast bands that are visible throughout the images. This is consistent throughout all the images and can be ignored as it is not over the area of interest in this study.

An increase in the number of images used for the HDR image does not result in a visually better final tone mapped image. This is particularly the case for a varied contrast window size. The smaller window size means each image in the HDR compilation contains less information. In comparison, the fixed contrast window provides a visually better image but due to the fixed window size, an increase in the number of images creates large amounts of repeated and redundant information.

The single image HDR results can also be used to evaluate the exposure value estimation. From Figures 4.2 and 4.4, it becomes obvious that the darker images correlate to a dimmer image in photography and similarly for brighter images - as shown by the EV selection (negative EV for darker images and positive EV for brighter images). Further visual comparisons of the images show visual improvement after the HDR tone mapping is applied.

The Lischinski et al. (2006) tone mapping is a local algorithm therefore it is able to bring about a higher contrast as seen in Figures 4.3(a) and 4.3(e). This is also the case for the Reinhard et al. (2002) algorithm and shown in Figures 4.3(c) and 4.3(g). The minor differences occur because the Reinhard algorithm applies a global luminance compression before the local adjustment. However, the local adjustment is still able to create a similar contrast enhancement as shown by the Lischinski algorithm.

The Ward histogram adjustment and normalising algorithms are both global algorithms so a lower contrast is expected. On inspection of Figures 4.3(b) and 4.3(d), the contrast is visibly lower than in Figures 4.3(a) and 4.3(c) with less detail in the cervical region and a darker and less visible C7/T1 junction. These are the figures with an appropriately estimated EV based on the brightness/darkness of the X-ray image. Considering the figures produced with EV of (0; 0; 0), the Ward histogram adjustment (Figure 4.3(h)) adapts better with the EV change as compared to the other tone mapping algorithms (Figures 4.3(e) - 4.3(g)). This is due to the compressed globally applied curve limit affecting a limited range whereas the normalise algorithm applies it throughout the entire range. The Reinhard algorithm applies a global luminance compression prior to the local adjustment thus achieving a similar result to the normalised image. The Lischinski creates a similar result as the objective of the algorithm is so obtain a final exposure (with the contrast reducing when all the images have identical EVs).

The built-in MatLab tone mapping is an enhancement of the Ward histogram adjustment algorithm. The contrast limited adaptive histogram equalisation is applied to the luminance channel (obtained form the logarithm and normalised HDR image). The image contrast is then further adjusted by specified parameters (left as default 1% of data which is saturated for increased contrast). This then produces an image similar to that of the Ward histogram tone mapping but with an improved contrast, as shown in Figure 4.2(a) and 4.4(a).

From Figure 4.6, it can be seen that as the voltage increases, the radiation penetration increases. Despite the lower attenuation (due to lack of water in the phantom), the figures show that varying information of the C7/T1 junction can be obtained with images at

different energy levels. From this, the single X-ray approach only considered scans of the phantom without water due to the lack of improvement in the C7/T1 junction without the added attenuation of water and from the results that support the dual energy approach.

4.2 Dual Energy HDR Results

The dual energy X-ray images were taken at all possible energy combinations for an exhaustive exploration. Each image pair was tested with the various image acquisition, HDR and tone mapping techniques. The contrast window sizes were varied as well as fixed for 3 images at each X-ray energy level. The exposure values were varied as for the single X-ray method, the energy combinations were varied and each tone mapping algorithm was applied to each HDR image. The results shown and analysed above are for selected images only. A total of 2835 images were produced in the testing phase of the 3 image and fixed contrast window size.

The dual energy scan uses two separate images of the same subject that are taken at different energy levels and is inspired by the approach taken by Sisniega et al. (2014) , which is explained in Section 2.5. Patient or object movement is not a concern as the scans are obtained in a single session with no variation or movement of the bones and the processing is limited to scans taken in the same session. In order to maximise the information obtained within the scans, each image is separated into 3 or 5 window images and then compiled as a single HDR image (a tonemapped image for each split image). Each of the HDR two images at different energy levels are combined to form an HDR image. This means that a 3-image HDR image consists of 6 contrast windows either with a constant or varied window size. The exposure values are allocated as per the single X-ray algorithm. As before, the figures shown in these results are a representative set of images to display the typical results.

4.2.1 Phantom without water

Figure 4.7 shows the original 80 kV and 145 kV scans of the phantom without water with the contrast window set over the entire contrast range. Figure 4.7(a) shows that with a lower voltage, despite the absence of water in the phantom, the humerus, scapula and clavicle create significant blockage for the C7/T1 junction. Figure 4.7(b) shows that at a much higher voltage the penetration of the radiation is considerably greater than that of Figure 4.7(a).

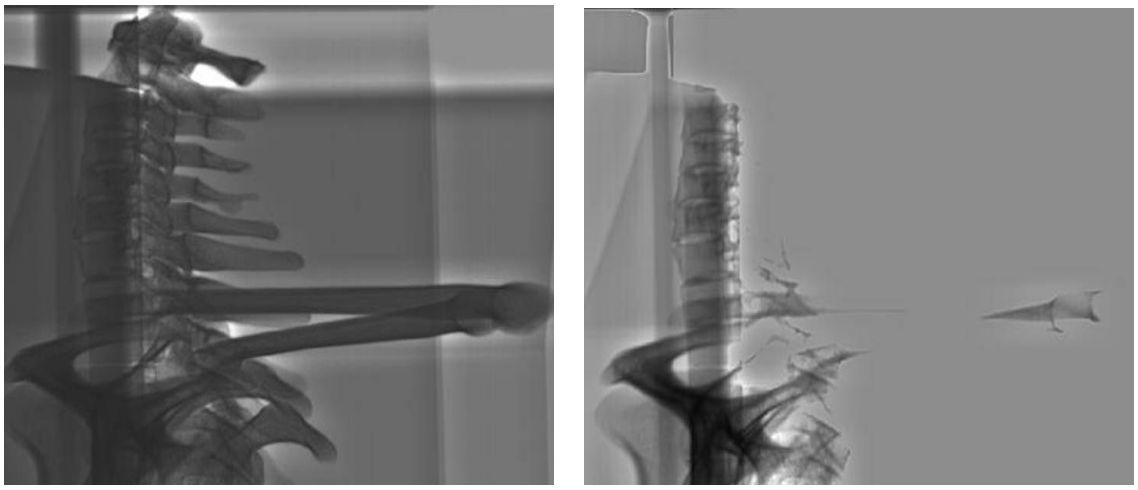

(a) 80 kV (b) 145 kV

Figure 4.7: Lucid original image showing full contrast window.

Figure 4.8 shows the MatLab tone mapping algorithm applied to the dual energy HDR image created from Figure 4.7. The maximum and minimum voltages are used in order to view the maximum differential attenuation of the two components being measured (soft tissue and bone) (Gulam et al., 2000; Sisniega et al., 2014). Figure 4.9 and 4.10 show the four tone mapping algorithms (Lischinski, Normailze, Reinhard and Ward histogram adjustment) applied to the 80 kV and 145 kV images. The exposure values indicate the minimum and maximum values assigned to the images within the HDR. The values range in steps of 2, as per Table 4.1.

From Figures 4.9 and 4.10, subjective evaluation indicates that the exposure values that offer the most information are from $-2; 0; 2$ to $-6; 0; 6$.

Figure 4.11 shows the results of the HDR tone mapping for a 90 kV and 140 kV scan with no Lucid, 5 images and varied contrast window size. The tone mapped results show images that contain no relevant or diagnostic information and the images appear dark and have poor contrast. The contrast window with 5 images produces a window size too small to contain significant information in the images used to create the HDR and final tone mapped image. These window sizes vary according to the contrast window size of each original image window to fit in 5 contrast windows. The resultant image produced does not provide any qualitative improvement on visualising the C7/T1 junction.

Given these poor results, the 5-image approach is not considered for further tests with dual energy images. The increased attenuation with water in the phantom will create further blockage of the C7/T1 junction. The Lucid, 3 image fixed contrast window approach is used for further testing where water is present in the phantom.

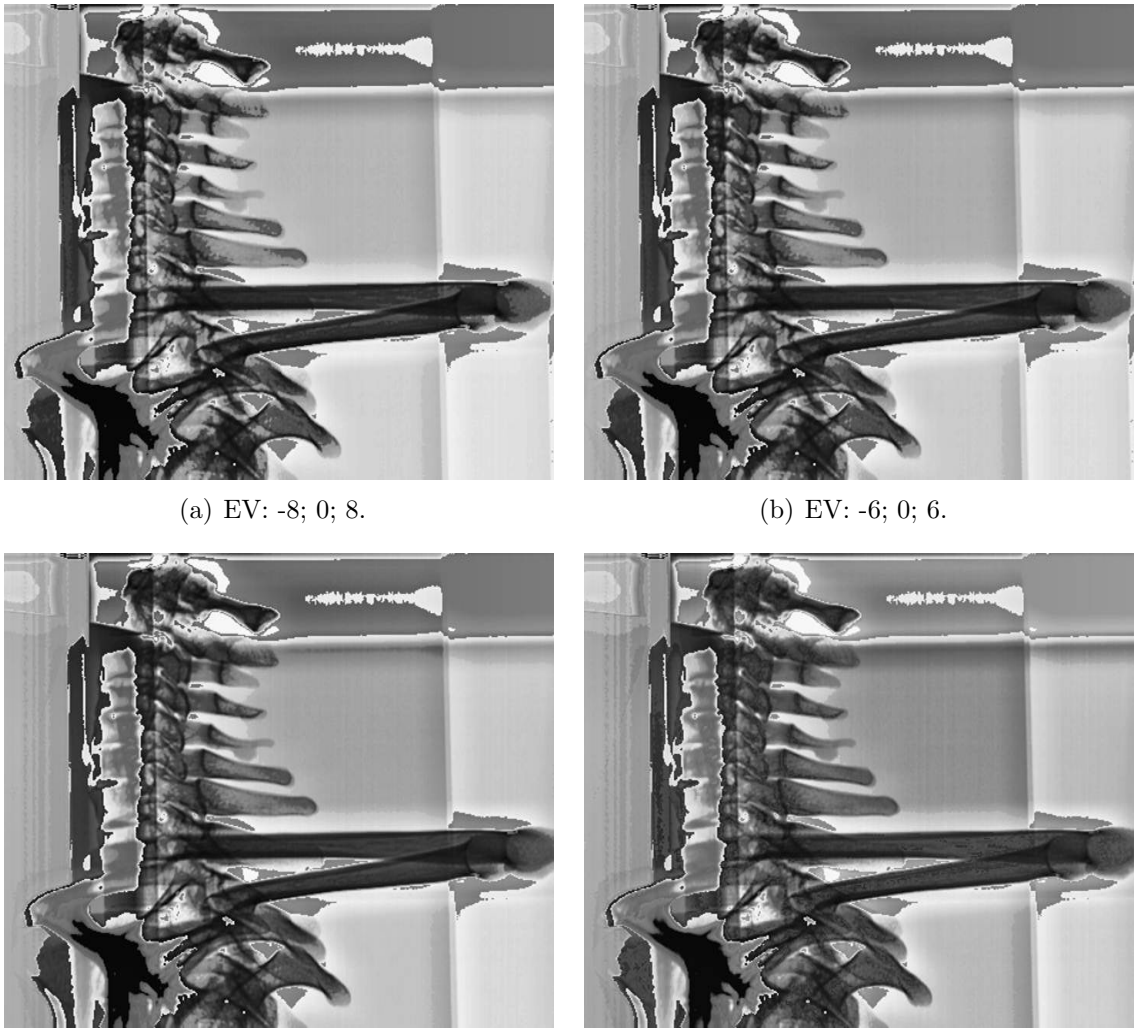

(a) EV: -8; 0; 8.

(b) EV: -6; 0; 6.

(c) EV: -4; 0; 4.

(d) EV: -2; 0; 2.

Figure 4.8: MatLab tone mapping algorithm of a 80 kV and 145 kV, Lucid, 3 image fixed window dual energy HDR image.

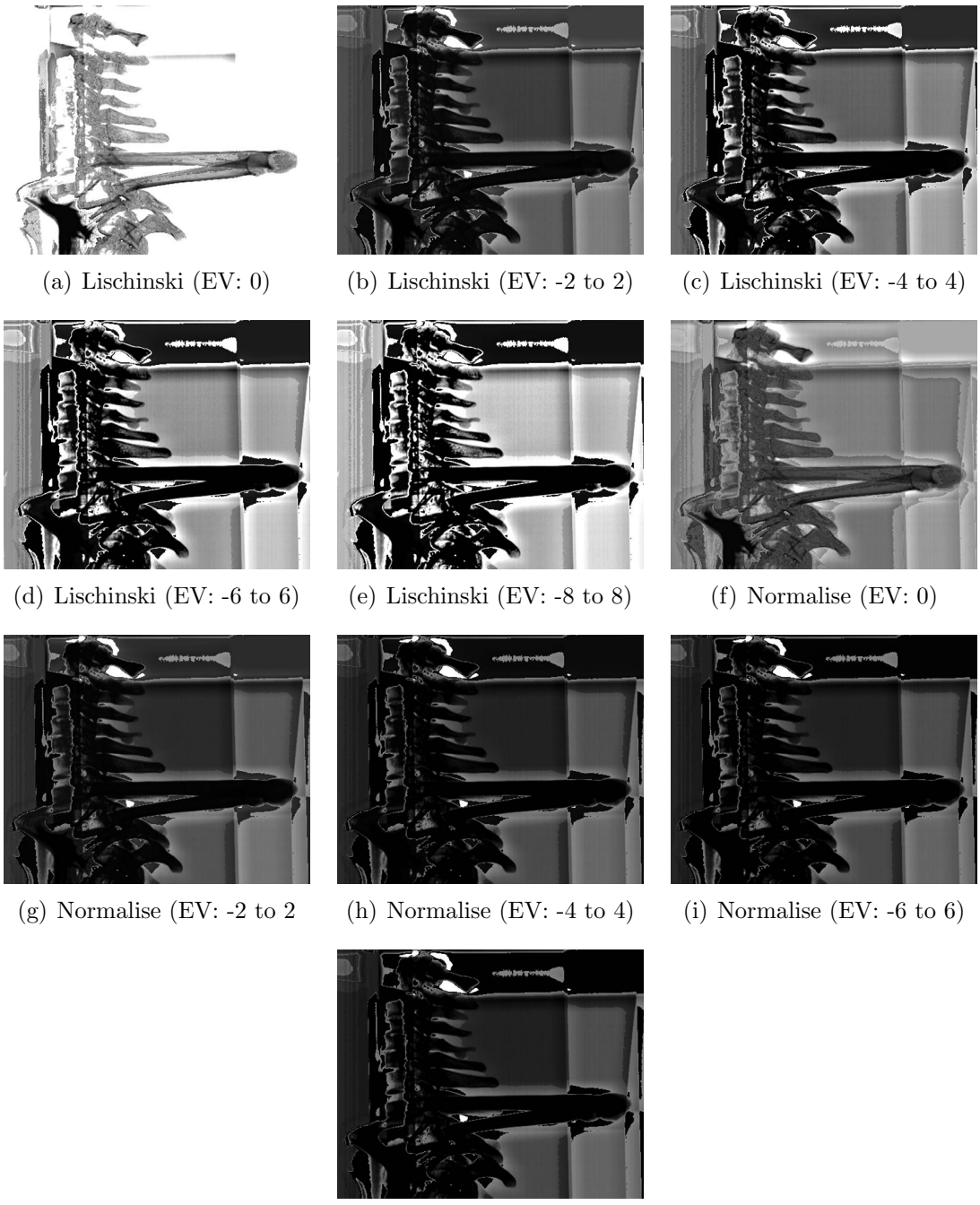

(a) Lischinski (EV: 0) (b) Lischinski (EV: -2 to 2) (c) Lischinski (EV: -4 to 4)

(d) Lischinski (EV: -6 to 6) (e) Lischinski (EV: -8 to 8) (f) Normalise (EV: 0)

(g) Normalise (EV: -2 to 2 (h) Normalise (EV: -4 to 4) (i) Normalise (EV: -6 to 6)

(j) Normalise (EV: -8 to 8)

Figure 4.9: Tone mapping of 80 kV and 145 kV, Lucid, 3 image fixed window dual energy HDR image.

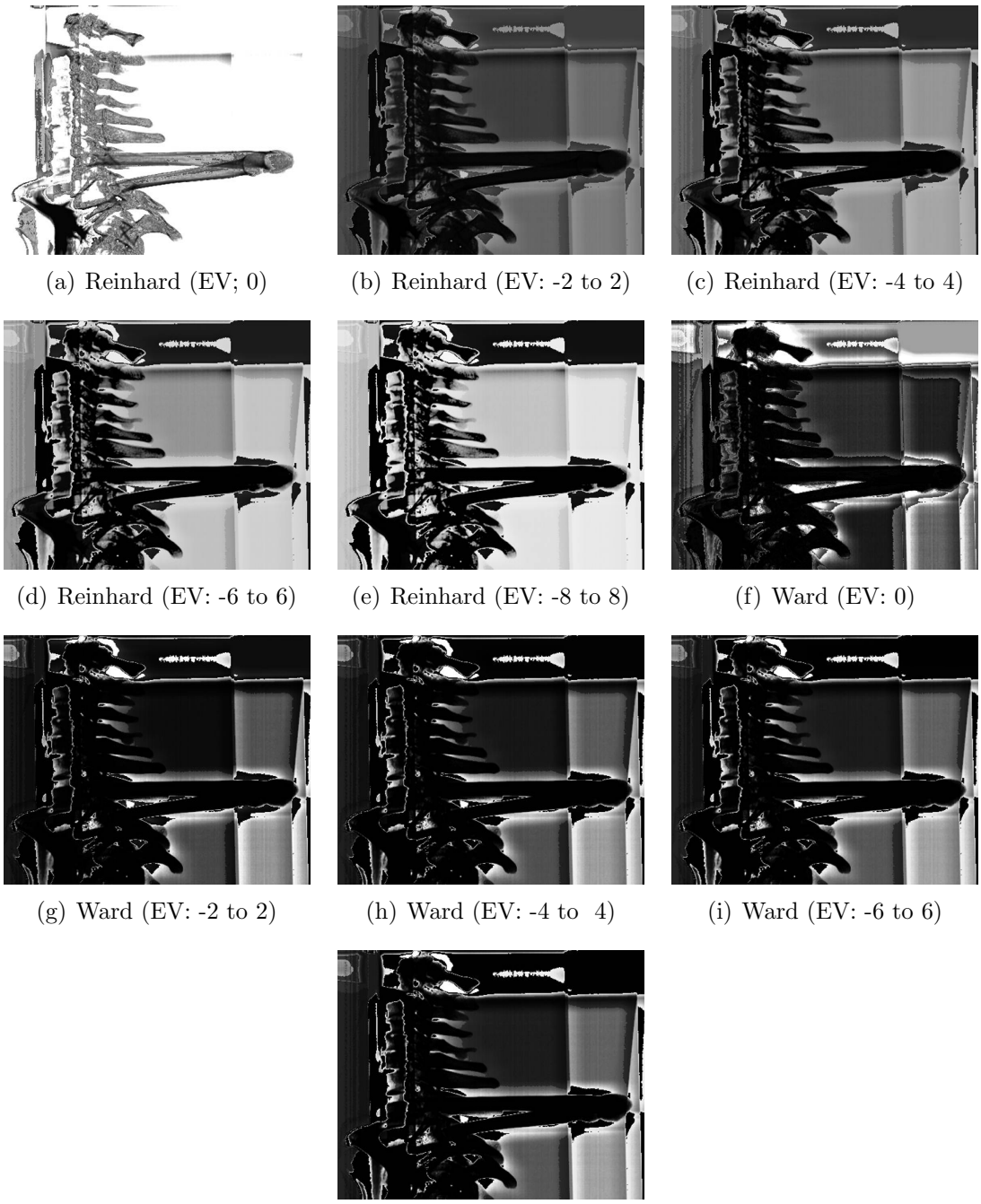

(a) Reinhard (EV; 0) (b) Reinhard (EV: -2 to 2) (c) Reinhard (EV: -4 to 4)

(d) Reinhard (EV: -6 to 6) (e) Reinhard (EV: -8 to 8) (f) Ward (EV: 0)

(g) Ward (EV: -2 to 2) (h) Ward (EV: -4 to 4) (i) Ward (EV: -6 to 6)

(j) Ward (EV: -8 to 8)

Figure 4.10: Tone mapping of 80 kV and 145 kV, Lucid, 3 image fixed window dual energy HDR images continued.

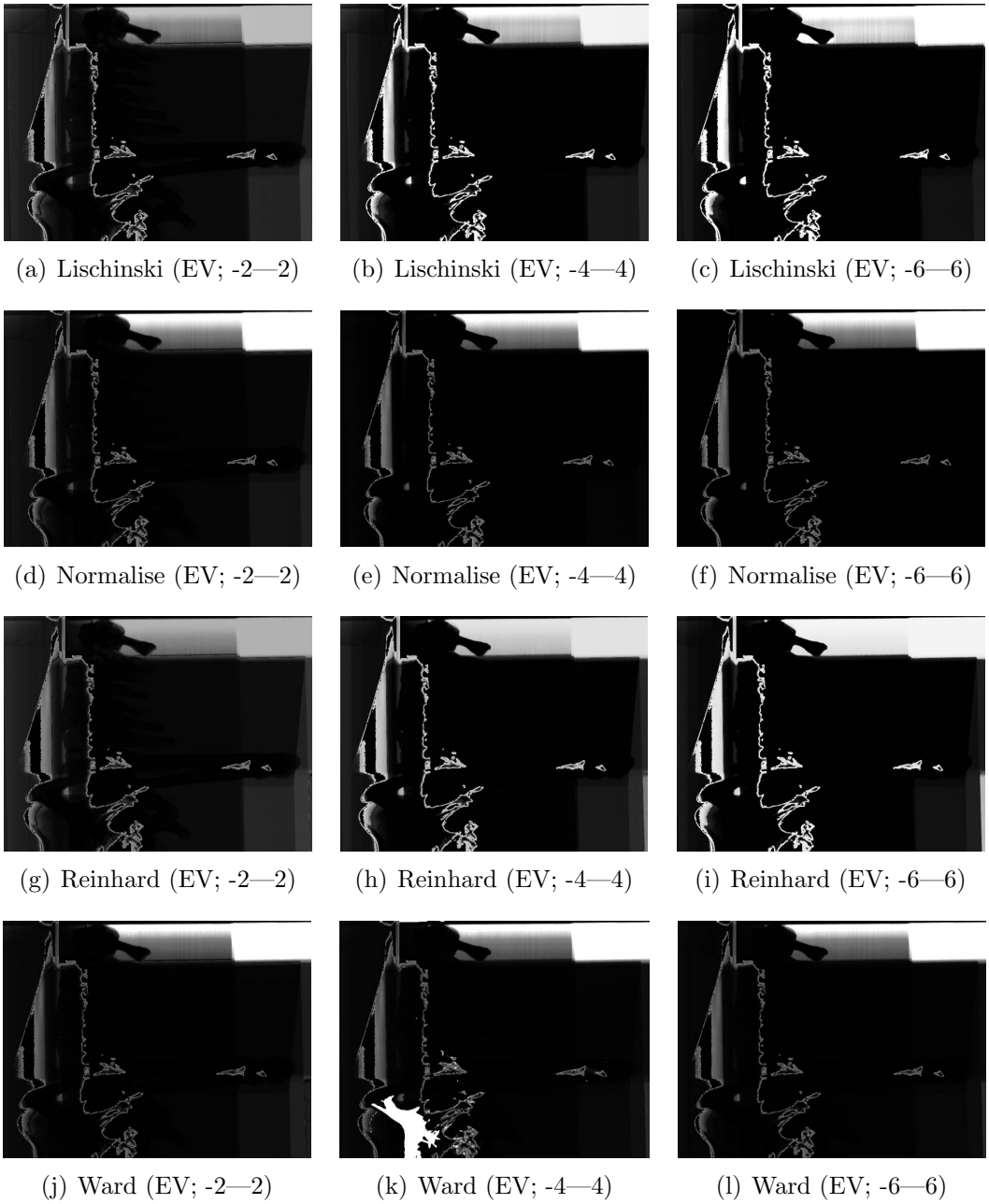

(a) Lischinski (EV; -2—2) (b) Lischinski (EV; -4—4) (c) Lischinski (EV; -6—6)

(d) Normalise (EV; -2—2) (e) Normalise (EV; -4—4) (f) Normalise (EV; -6—6)

(g) Reinhard (EV; -2—2) (h) Reinhard (EV; -4—4) (i) Reinhard (EV; -6—6)

(j) Ward (EV; -2—2) (k) Ward (EV; -4—4) (l) Ward (EV; -6—6)

Figure 4.11: Tone mapping of 90 kV and 140 kV, Lucid, 5 image varied window dual energy HDR images continued.

The results above provide a view on the dual energy and HDR tone mapping effect on images of the phantom. The results have been analysed qualitatively based on the visual clarity of the C7/T1 junction. For the images obtained of the phantom without water covering the vertebrae, the following can be said:

- Obstructions were caused by shoulder girdle (but not by soft tissue).
- Lower energy X-ray image revealed superficial bones.
- Higher energy X-ray image revealed deeper bones.

The above results are all as expected. The HDR images were produced from the built in MatLab HDR and various tone mapping algorithms from scans at various energy levels. These results are based on the scans obtained of the phantom without water - thus a lowered attenuation. This lowered attenuation does not accurately represent an actual shoulder girdle. Therefore the phantom needs to be filled with water and the HDR and tonemapping techniques repeated.

4.2.2 Phantom with water

Figure 4.12 shows the original phantom scan with water covering the vertebrae, Lucid on and contrast window over the entire range. These images showing the entire contrast range decreases the image quality from the usual Lodox lateral scan results as they include the initial and final contrast ranges usually removed to sharpen the details. Figure 4.12(a) is at 80 kV, Figure 4.12(b) is at 145 kV and Figure 4.12(c) is at 120 kV. From this figure, it can be seen that no valuable diagnostic information can be obtained from these sources. This is because the entire contrast range is selected and viewed. This does not allow the contrast levels to be isolated for certain regions. The attenuation at the C7/T1 junction is greatly intensified with the addition of water to the phantom and the images produced are of a much lower quality. Images were produced for each dual energy pairing at all EV's. The number of images produced for each pairing is summarised in Table 4.2. Note that this table does not include the images produced by the tone mapping algorithms. Each dual energy pair produces 9 images with varying EV's - each energy level produces images for EVs ranging from (-8; 0; 8) to (8; 0; -8) in steps of +2 or -2. This allows for a holistic view on the capabilities of the tone mapping algorithms.

For the lowest ($80kV$) and highest ($145kV$) energy levels, results are shown in Figure 4.13. The results are not diagnostically useful. The somewhat more detailed results from

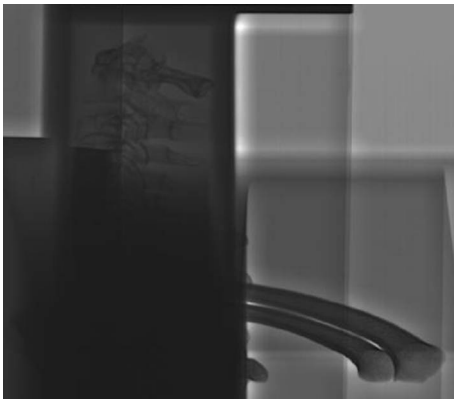

(a) Original phantom scan at 80 kV

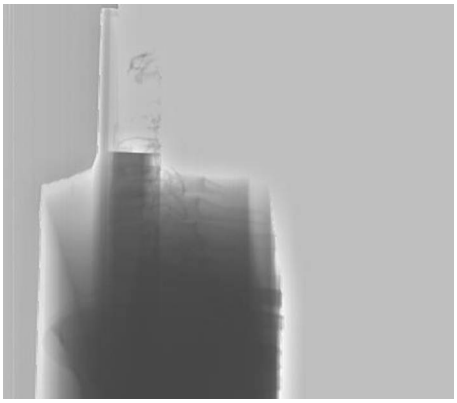

(b) Original phantom scan at 145 kV

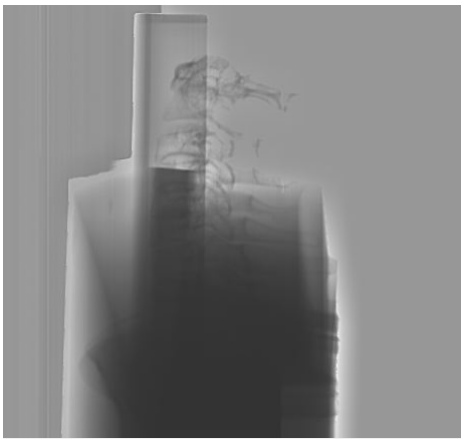

(c) Original phantom scan at 120 kV

Figure 4.12: Original phantom scan with water, Lucid and entire contrast window.

Table 4.2: Dual energy pairings.

Higher Energy (kV)	**90**	**100**	**110**	**120**	**130**	**135**	**140**	**145**
Lower Energy (kV)								
80	✓	✓	✓	✓	✓	✓	✓	✓
90		✓	✓	✓	✓	✓	✓	✓
100			✓	✓	✓	✓	✓	✓
110				✓	✓	✓	✓	✓
120					✓	✓	✓	✓
130						✓	✓	✓
135							✓	✓
140								✓

EV's [-2 to 2] to [-6 to 6] suggest that the optimal EV choice thus lies between these figures and results therein are further explored. The results show that the highest and lowest energy levels do not combine to produce a useful image. The results are unable to produce a diagnostically useful result.

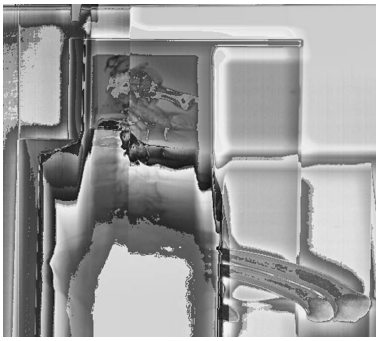

(a) EV: 0

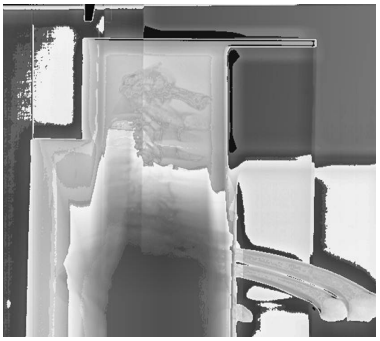

(b) EV: -8; 0; 8

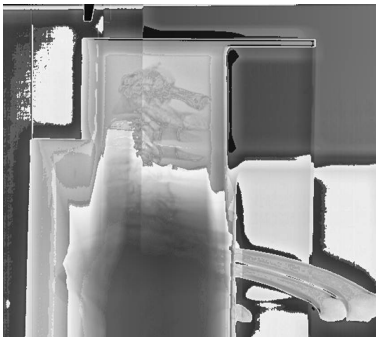

(c) EV: -6; 0; 6

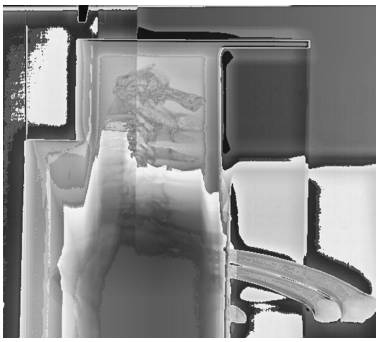

(d) EV: -4; 0; 4

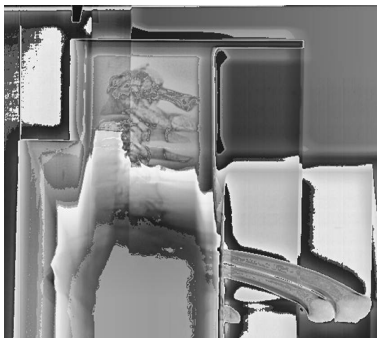

(e) EV: -2; 0; 2

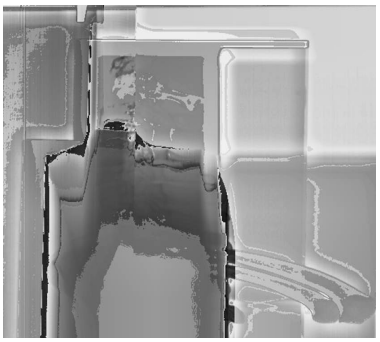

(f) EV: 2; 0; -2

(g) EV: 4; 0; -4

(h) EV: 6; 0; -6

(i) EV: 8; 0; -8

Figure 4.13: Dual Energy HDR of 80 kV and 145 kV scans with Lucid, 3 images and fixed contrast window.

To further analyse the results, dual energy images at a constant 80 kV lower energy, with exposure value 0, Lucid applied and using the MatLab tone-mapping algorithm are shown in Figure 4.14. The images produced from the 80 kV to 110 kV energy levels upwards are very noisy. The images do not provide an improved qualitative visualisation of the lower cervical vertebrae at the higher dual energy differences.

(a) 80 - 90 kV with EV:0

(b) 80- 100 kV with EV:0

(c) 80 - 110 kV with EV:0

(d) 80 - 120 kV with EV:0

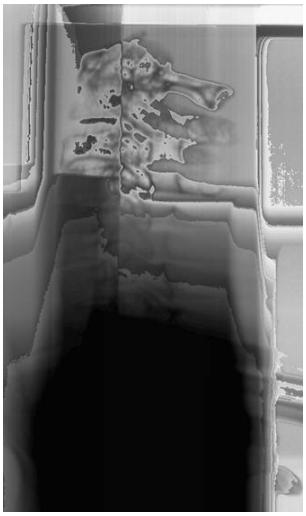

(e) 80 - 135 kV with EV:0

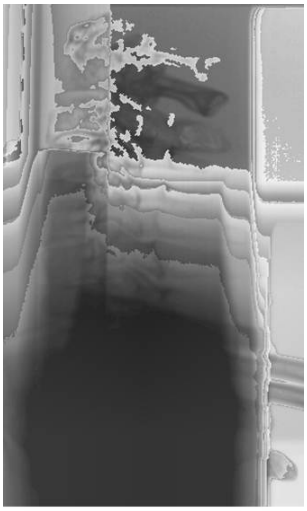

(f) 80 - 140 kV with EV:0

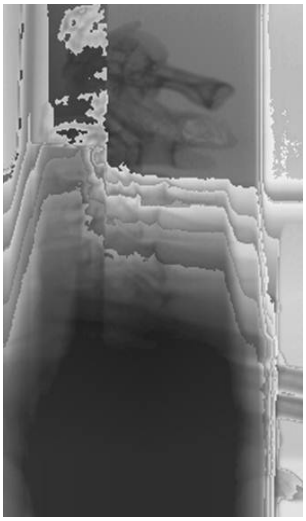

(g) 80 - 145 kV with EV:0

Figure 4.14: Dual energy HDR images with 80 kV lower energy, EV 0, Lucid applied and using the MatLab tone-mapping algorithm.

Consider Figure 4.15 which shows dual energy HDR images with 3 image, fixed window, no Lucid, 80 - 120 kV, tone mapped with the built in MatLab algorithm at various exposure values. Here, too, no useful images are produced.

The dual energy HDR images are not only constructed using 80 kV as the lower band energy. As described in Table 4.2, the lower energy is varied. This is to show the effect of increasing the X-ray energy levels for the dual energy HDR. Figures 4.16, 4.17 and 4.18 respectively show selected HDR results using 3 images, fixed window sizes, Lucid applied and the MatLab tone-mapping algorithm:

- 90 kV - 110 kV
- 100 kV - 120 kV
- 110 kV - 130 kV

4.2.3 Discussion

The results of the HDR processing of the phantom without water indicate that the MatLab tone map algorithm, in comparison to the Lischinski, Normalisation, Reinhard and Ward algorithms, provides the qualitatively better image. The local property of the Lischinski algorithm was demonstrated for both the single and the dual energy cases and resulted in higher contrast, more so in the dual energy case. The improvement is not diagnostically useful, based on visual inspection.

Normalising the images for tone mapping created a darkening image and lower contrast as the EV increased. This loss in visibility of the cervical spine region becomes evident, as shown in Figures 4.10(f) to 4.10(j). The images produced by this algorithm are very dark and fail to produce a visible improvement at the junction.

From Figures 4.9 and 4.10, it can be seen that the Reinhard tone mapping algorithm's global luminance compression and local adjustments achieve a similar result to that of the Lischinski algorithm. Similar contrast traits are exhibited by both result sets. However, the extra global luminance compression performed by the Reinhard allows for a smoother image to be produced instead of having such rapid intensity changes across all EVs as seen in the Lischinski. These images at the correct EVs provide a slight improvement in the visual quality of the C7/T1 junction. However, this is not diagnostically useful.

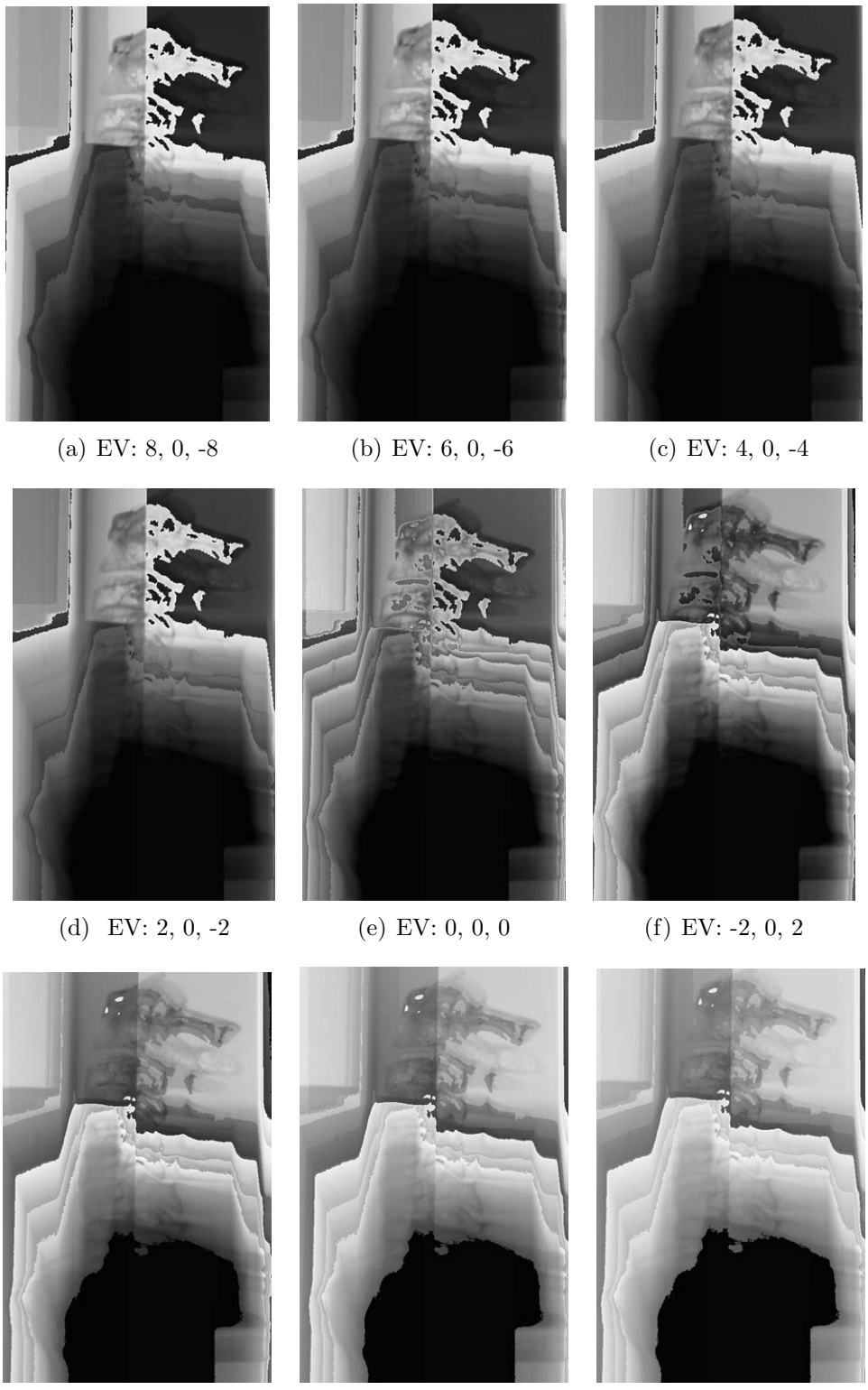

(a) EV: 8, 0, -8 (b) EV: 6, 0, -6 (c) EV: 4, 0, -4

(d) EV: 2, 0, -2 (e) EV: 0, 0, 0 (f) EV: -2, 0, 2

(g) EV: -4, 0, 4 (h) EV: -6, 0, 6 (i) EV: -8, 0, 8

Figure 4.15: Dual energy HDR images with 3 image, fixed window, no Lucid, 80 - 120 kV, tone mapped with the built in MatLab algorithm at various exposure values.

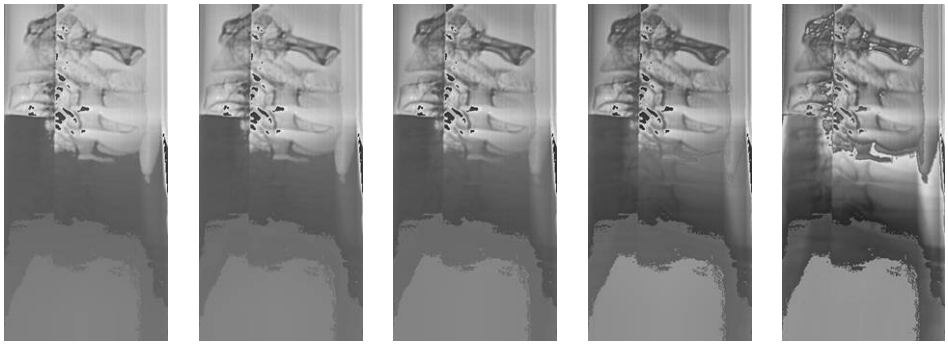

(a) EV: 8, 0, -8 (b) EV: 6, 0, -6 (c) EV: 4, 0, -4 (d) EV: 2, 0, -2 (e) EV: 0, 0, 0

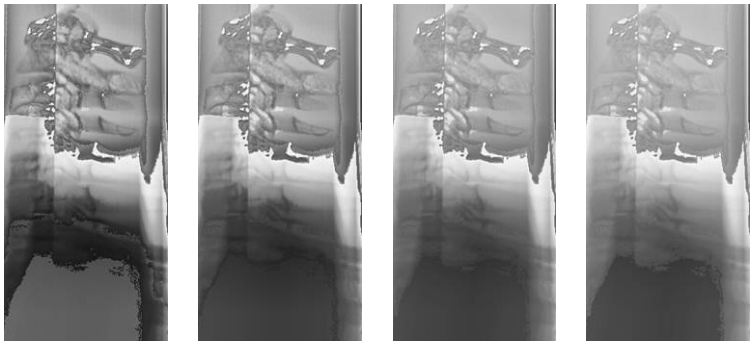

(f) EV: -2, 0, 2 (g) EV: -4, 0, 4 (h) EV: -6, 0, 6 (i) EV: -8, 0, 8

Figure 4.16: 3 image, fixed window, Lucid applied HDR dual energy (90 - 110 kV) image tone mapped with the built-in MatLab algorithm at various exposure values.

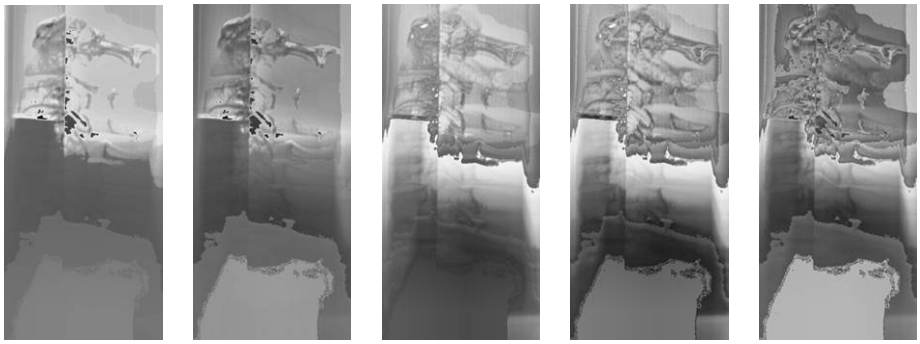

(a) EV: 8, 0, -8 (b) EV: 6, 0, -6 (c) EV: 4, 0, -4 (d) EV: 2, 0, -2 (e) EV: 0, 0, 0

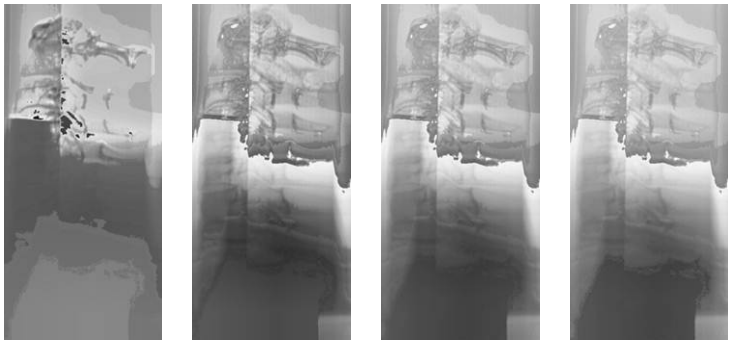

(f) EV: -2, 0, 2 (g) EV: -4, 0, 4 (h) EV: -6, 0, 6 (i) EV: -8, 0, 8

Figure 4.17: 3 image, fixed window, Lucid applied HDR dual energy (100 - 120 kV) image tone mapped with the built-in MatLab algorithm at various exposure values.

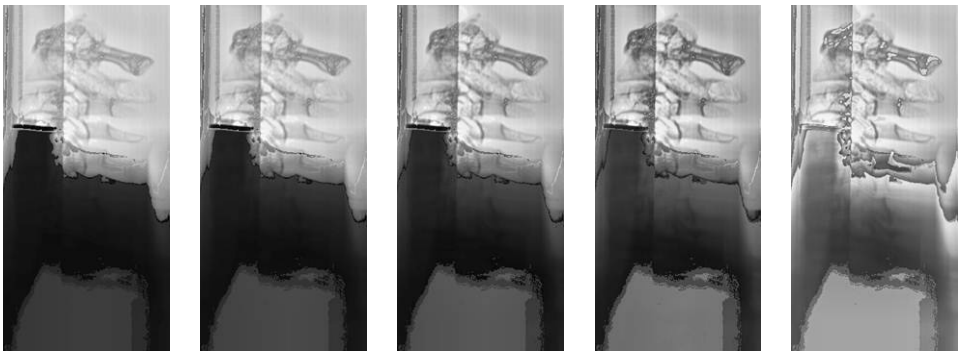

(a) EV: 8, 0, -8 (b) EV: 6, 0, -6 (c) EV: 4, 0, -4 (d) EV: 2, 0, -2 (e) EV: 0, 0, 0

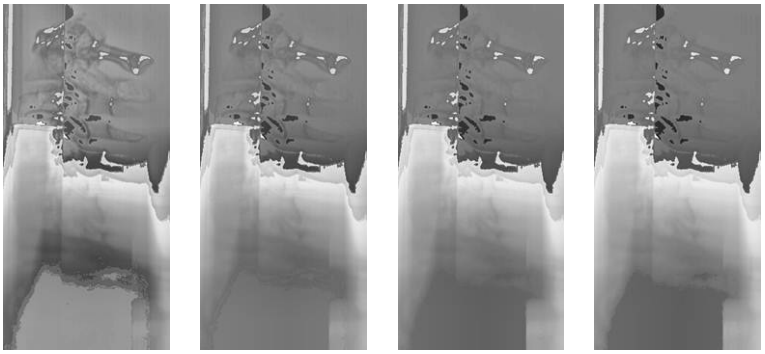

(f) EV: -2, 0, 2 (g) EV: -4, 0, 4 (h) EV: -6, 0, 6 (i) EV: -8, 0, 8

Figure 4.18: 3 image, fixed window, Lucid applied HDR dual energy (110 - 130 kV) image tone mapped with the built-in MatLab algorithm at various exposure values.

The Ward tone mapping/histogram adjustment algorithm provides a similar result to that of normalisation. Both global algorithms create a darker image, although Ward provides a better contrast of the vertebrae - greater difference between the areas around the bone and background. The HDR characteristic of using values throughout the dynamic range causes the improved visible range but fails to enhance the C7/T1 junction.

The 5-image, no Lucid and varied contrast window size images approach was also tested with the dual energy HDR method. As previously discussed, the contrast window is too small and the images produced are extremely dark and provide no valuable information. This situation is similar to that of the single image case. Thus it can be concluded that the use of a varying contrast non-overlapping windows for HDR applied to X-ray images does not provide any improvement in image quality or the visibility of the C7/T1 junction.

Furthermore, after the results for the various tone mapping algorithms are analysed, it becomes clear that the built-in MatLab tone mapping algorithm provides the most desirable result albeit among results that are not diagnostically useful. The Lischinski, Ward and normalisation algorithms provided an improvement from the single X-ray tone mapping but failed to produce an improved C7/T1 junction. The Reinhard algorithm provided a better isolation of bone vs. background image but also did not enhance the C7/T1 junction. It should be noted that these results were for images taken of the phantom without the additional attenuation created by water to mimic soft tissue.

The HDR method used in photography aims to increase the dynamic range of an image by combining the dynamic ranges of various images. Tone mapping is used to compress the HDR image into a narrow enough range to be visible or displayed. This concept was recreated with a dual energy X-ray image and analysed. The results of the dual energy HDR tone mapped X-ray image have revealed:

- The exposure value does have an impact on the visual appearance of an image, although the resulting images are of poor quality.
- The dual energy HDR technique with dual energy images is unable to enhance the C7/T1 junction.

The exploration using HDR and tonemapping has not been able to provide any visual improvement of the C7/T1 junction. From here, the exploration moves toward the isolation of each region independently to see whether the HDR tonemapping technique can provide any improvement that is not focused on the junction.

4.3 Region of Interest HDR Results

Based on the results and findings of the single and dual energy HDR studies, the region of interest (ROI) analysis is concentrated on images with the following attributes:

- Phantom with water.
- 3 images.
- Fixed contrast window sizes.
- Lucid on.
- MatLab tone mapping algorithm.
- All EV ranges.
- Dual energy HDR.

The number of images and contrast window size were selected due to the poor results shown with 5 images and varying contrast window sizes in both the single and dual energy studies. The Lucid state and tone mapping algorithm are based on the best results in the dual energy analysis.

The region of interest focuses on the cervical and thoracic regions individually. The two regions of interest are isolated to maximise the information obtained from each scan. The scans are isolated by selecting the cervical and thoracic regions from the same set of X-ray scans and individually processed by the HDR. Figure 4.19 shows the isolated regions in comparison to the normal lateral scan obtained.

Figure 4.20 shows the entire region in 80 kV - 100 kV dual energy HDR images. Figure 4.21 shows the thoracic region of 100 kV - 120 kV dual energy HDR images. These images show that the exposure values that produce an improvement in the visualisation of the cervical and thoracic regions are above the EV set of [-2; 0; 2]. Figure 4.22 explores the isolated cervical region with EVs at [-6; 0; 6] with an 80 kV lower energy and various higher dual energy pairings. This EV set is chosen because Figure 4.20 shows that it produces the clearest view out of the images within the result set.

The cervical region images seen in Figure 4.22 and the thoracic region in Figure 4.23 show the effects of different energy levels on the region's visualisation. The cervical

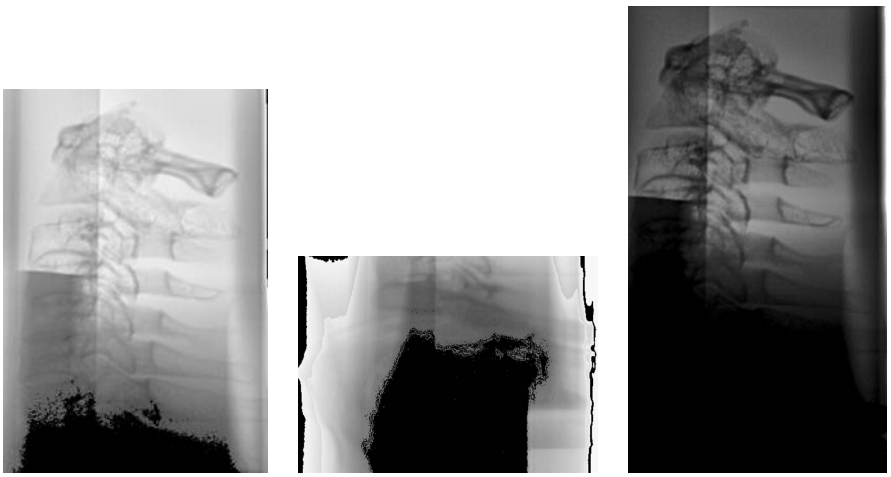

(a) Cervical region (b) Thoracic region (c) Entire region

Figure 4.19: Comparison between the isolated regions, (a) and (b), and the normal lateral scan, (c).

image shown uses a 80 kV lower energy level whilst the thoracic uses a 100 kV lower energy level for the HDR dual energy algorithm. These results show various dual energy combinations with a fixed EV set of [-6; 0; 6]. The results differ in comparison to the results where the dual energy combination is constant and the EV sets are varied (see Figures 4.20 and 4.21 for examples of images produced at other EVs for comparison).

The thoracic region, even after isolation and applying dual energy analysis at the highest energy scan, does not improve in the visualisation of the C7/T1 junction. The exploration of the C7/T1 junction has shown that using the built in MatLab HDR and tone mapping algorithm does not offer an improvement on its visualisation. The highest energy (for greatest penetration) is unable to be maximised by the HDR tone mapping methodology to extract further useful information within the junction.

However, the cervical images do produce a clear image of the cervical vertebrae. A signal to noise ratio analysis is done on this region in order to examine how this compares to an image produced without HDR processing.

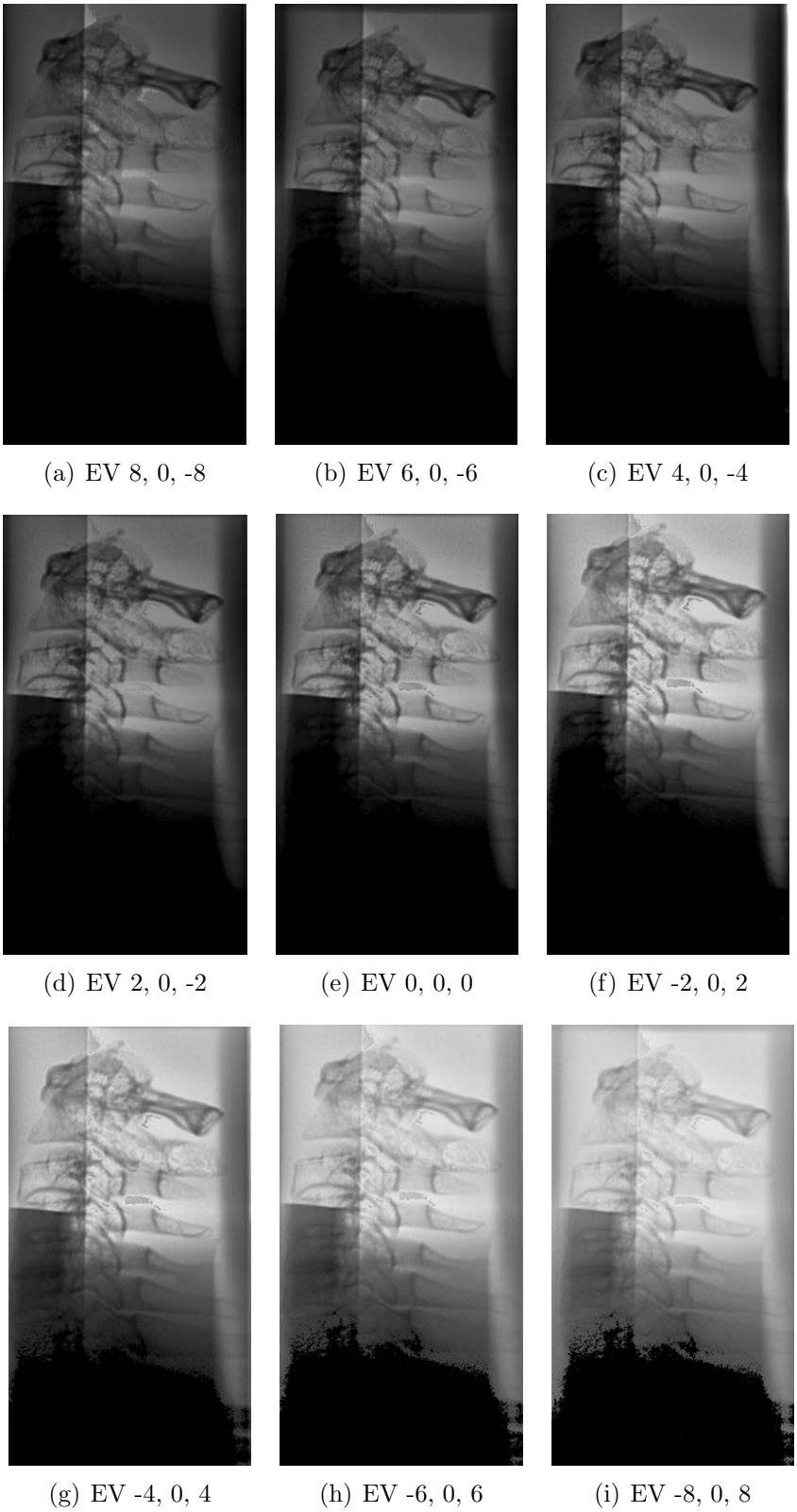

(a) EV 8, 0, -8 (b) EV 6, 0, -6 (c) EV 4, 0, -4

(d) EV 2, 0, -2 (e) EV 0, 0, 0 (f) EV -2, 0, 2

(g) EV -4, 0, 4 (h) EV -6, 0, 6 (i) EV -8, 0, 8

Figure 4.20: Entire region of 80 kV - 100 kV dual energy HDR.

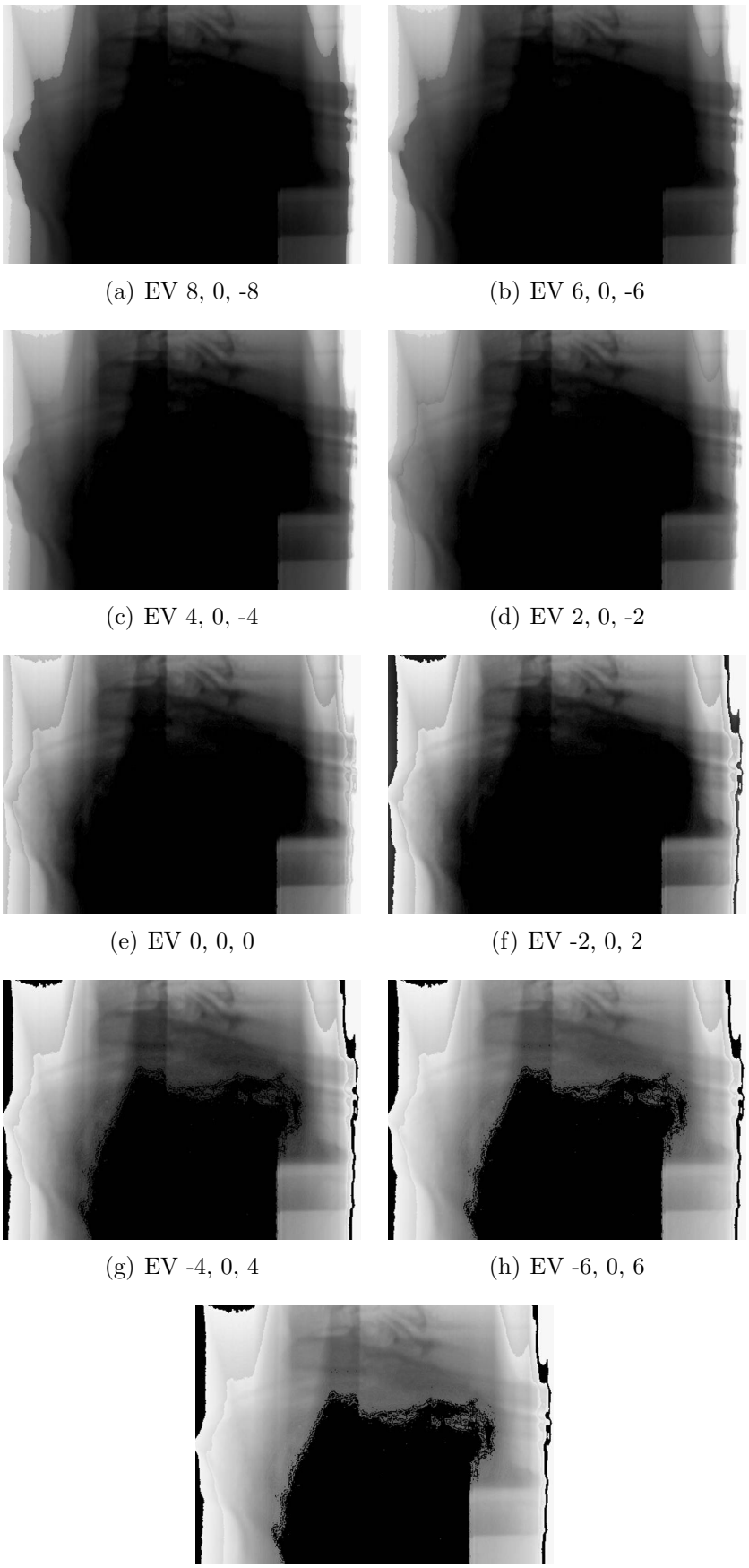

(a) EV 8, 0, -8

(b) EV 6, 0, -6

(c) EV 4, 0, -4

(d) EV 2, 0, -2

(e) EV 0, 0, 0

(f) EV -2, 0, 2

(g) EV -4, 0, 4

(h) EV -6, 0, 6

(i) EV -8, 0, 8

Figure 4.21: Thoracic region of 100 kV - 120 kV dual energy HDR.

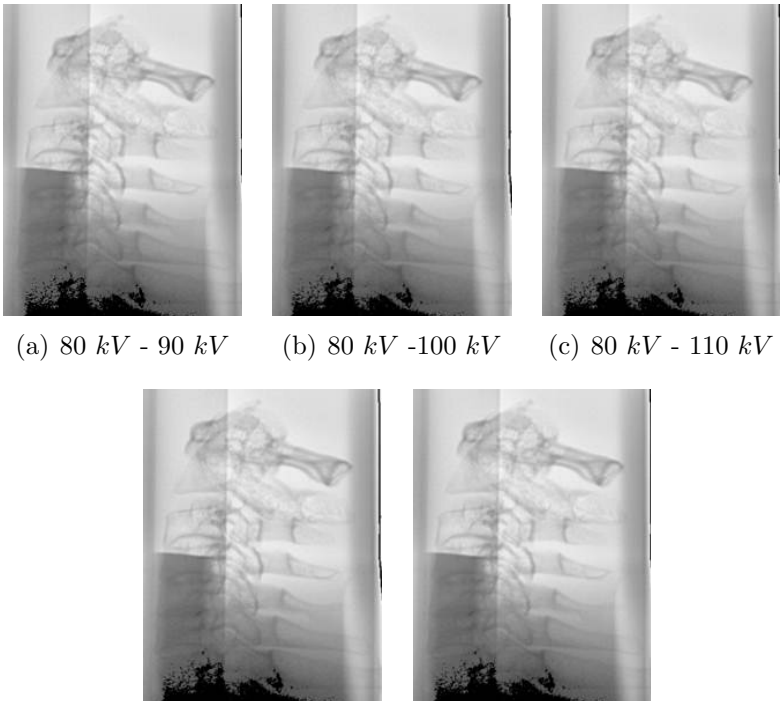

(a) 80 kV - 90 kV (b) 80 kV -100 kV (c) 80 kV - 110 kV

(d) 80 kV - 120 kV (e) 80 kV - 130 kV

Figure 4.22: Cervical region of 80 kV lower energy for a dual energy HDR at EV [-6; 0; 6].

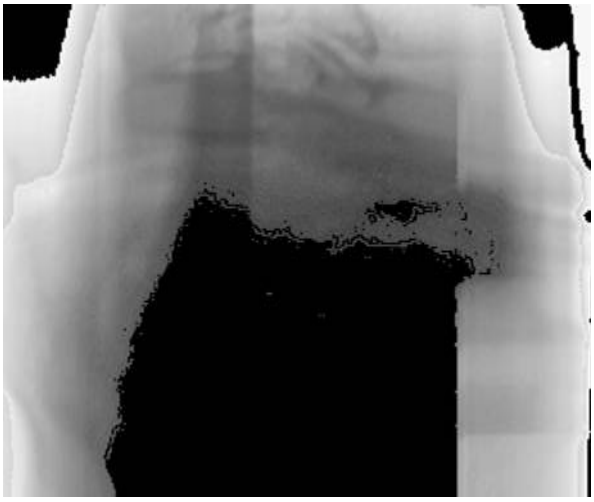

(a) 120 kV - 130 kV

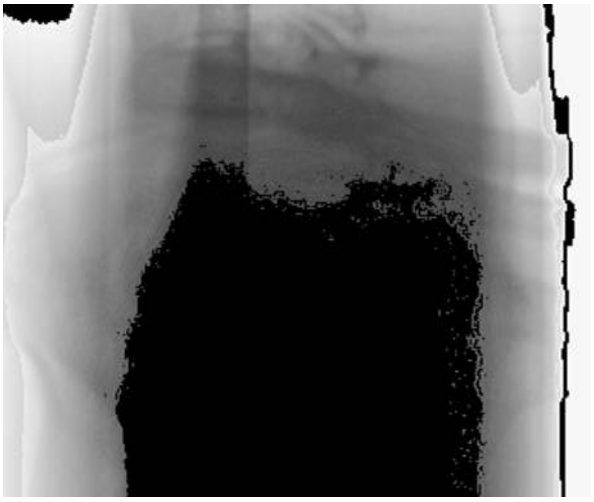

(b) 120 kV -140 kV

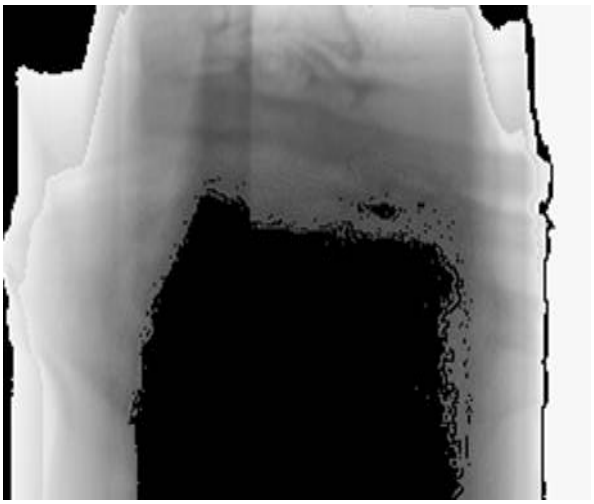

(c) 120 kV - 145 kV

Figure 4.23: Thoracic region of 120 kV lower energy for a dual energy HDR at EV [-6; 0; 6].

4.3.1 Cervical region signal to noise analysis

The signal-to-noise ratio (SNR) was calculated for the cervical region HDR images and compared against the reference images as described in Section 3.5.1. The reference images can be found in Figure 4.24. The reference images were obtained with Lucid applied and without the shoulder girdle or water present - thus minimising the attenuation across the C7/T1 junction.

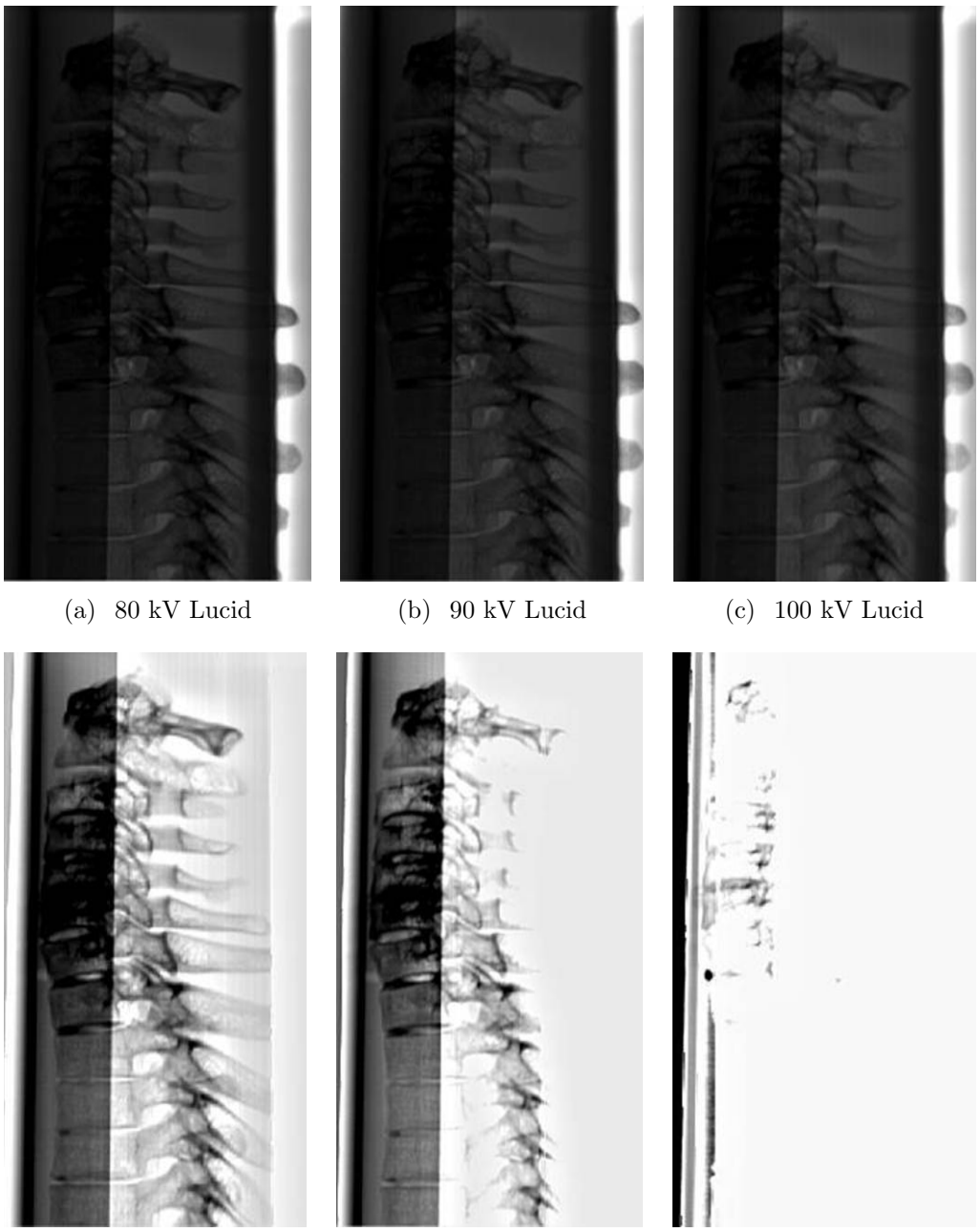

(a) 80 kV Lucid (b) 90 kV Lucid (c) 100 kV Lucid

(d) 110 kV Lucid (e) 120 kV Lucid (f) 130 kV Lucid

Figure 4.24: Reference images of the cervical and thoracic vertebrae at different kV levels with Lucid applied.

The reference image was chosen to be at 110 kV due to its energy level which did not wash out the cervical vertebrae. The reference image and the HDR images were obtained under the same imaging conditions. The images were cropped in order to contain only the cervical region for SNR analysis.

The cropped reference image corresponding to the cervical region isolated for ROI analysis is shown in Figure 4.25.

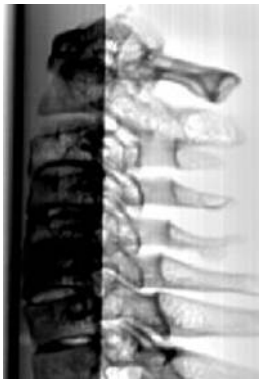

Figure 4.25: 110 kV Lucid cervical reference image for SNR analysis.

The following energy combinations were assessed:

- 80 - 90 kV
- 80 - 100 kV
- 80 - 110 kV
- 80 - 120 kV
- 80 - 130 kV
- 90 - 110 kV
- 100 - 120 kV

The SNR values are plotted in Figures 4.26 and 4.27. These figures show the calculated SNR values for each EV selection at the various energy combinations used to visualise the cervical region. The results have been separated into 2 figures in order to show the SNR results for all the 80 kV lower energy scans. The highest SNR is produced at 80 - 90 kV at EV[-8; 0; 8]. This is followed by the 80 - 120 kV combination at the same EV. The lowest overall SNR value per EV is produced by the 80 - 90 kV combination. The SNR results confirm the reliance on EV selection.

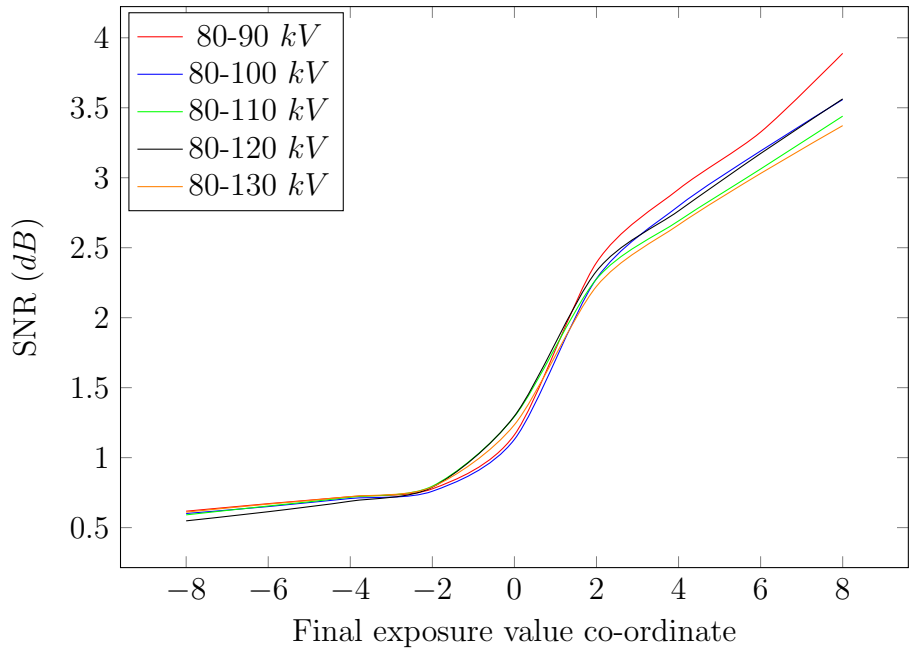

Figure 4.26: SNR results at the various EV's for the cervical dual energy scan of 80 kV lower energy and 90 kV - 130 kV higher energy against the 110 kV reference image with Lucid applied. The final EV for the set of 3 is shown, e.g. the -8 in the set of [8; 0; -8] EV's.

With the above results, the energy combinations that produced the highest SNRs are evaluated further with other energy combinations. This is to provide an exhaustive exploration of the various cervical energy level combinations to see which will provide the highest SNR result. The 90 kV energy is paired as the lower energy with 110 kV while the 120 kV is paired as the higher energy with 100 kV.

The SNR results are shown in Figure 4.27. These results exhibit a similar trend to the previous SNR figures. From these results, it would appear that the higher the EV, the higher the SNR.

The highest SNR is produced at EV's [-8; 0; 8] for the 100 - 120 kV cervical image, as shown in Figure 4.28. These energy levels correspond to the Lodox scans for a large C-spine and medium thoracic lumbar spine (Table 3.1). Considering the reference images in Figures 4.24(c) and 4.24(e) which are at the same energy levels as the dual energy combination used by the HDR, the result, which used scans of the phantom containing water (unlike the reference images) produces an image that combines and extracts information from both the 100 kV and 120 kV images into a single image.

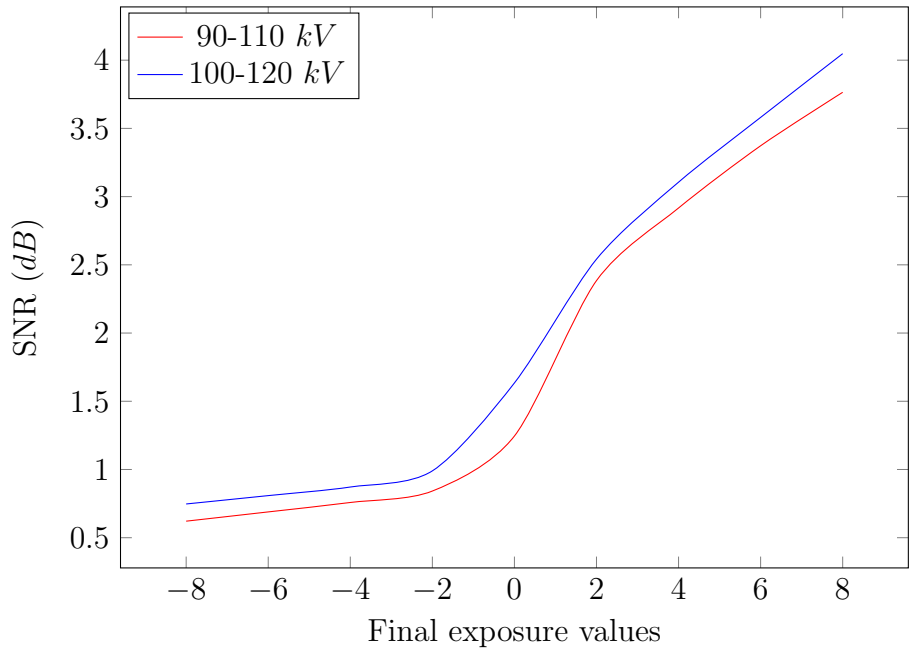

Figure 4.27: SNR results at the various EV's for the cervical dual energy scan of 90 and 100 kV lower energy and 110 and 120 kV higher energy against the 110 kV reference image with Lucid applied.

Figure 4.28: 100 kV - 120 kV dual energy HDR result at EV [-8; 0; 8].

4.3.2 Discussion

The EV selection plays an important role in the HDR images produced. Noting the previous result of optimal EVs being between [-2; 0 ; 2] and [-6; 0; 6] from visual inspection, the images produced in Figures 4.22 & 4.23 produce optimal results from EV's of [-2; 0; 2] and higher. This is shown by the increasing SNR results of the HDR images as the EV's increase between this range.

The built-in MatLab tone mapping algorithm uses an enhanced histogram compression of pixels in sparsely populated regions (Larson et al., 1997; MathWorks, 2017). The algorithm can be summarised as (Larson et al., 1997):

1. Compute sample and overlay images.
2. Add sample and overlay to original image.
3. Blur local image based on visual acuity function.
4. Generate histogram of image.
5. Adjust histogram to contrast sensitivity function.
6. Apply histogram adjustment to image.
7. Convert image to RGB display.

Step 3 applies an adjustment onto the HDR image that attempts to interpolate pixel values in order to show higher resolution in brighter areas whilst lower in the darker areas. Step 5 is based on a linear ceiling and a human contrast sensitivity histogram adjustment algorithm. The algorithm effectively interpolates and maps the display brightness between the image and the linear ceiling using a specified function (Larson et al., 1997). When this is applied to the dual energy scans, it produces an image that has the darkest and brightest regions highlighted. This then creates an image that contains an extrapolated version of the darkest and brightest regions which maintains greater amounts of information.

The ROI analysis applying this tone mapping algorithm shows that the cervical image can be isolated and a useful image produced. The thoracic region contains no useful information. The SNR analysis was performed on the cervical region against a reference image obtained of the same phantom. The SNR analysis enabled quantitative exploration of the effects of energy combination on HDR results.

The HDR tone mapping combined with a region of interest analysis aimed to produce an enhanced image of the C7/T1 junction. The results do not show a diagnostically useful image with clear junction visualisation. The isolation of each region revealed that the cervical region could be enhanced but not the thoracic.

4.4 Summary

A summary of the sequence and processing for the exploration of the C7/T1 junction using HDR and tone mapping techniques is shown in Figure 4.29.

Three categories of image were acquired for processing. These are single image (without water) and dual energy (without and with water).

The single image HDR without water in the phantom showed that the increase in number of images, whilst decreasing each contrast window, does not create an HDR image that can be tone mapped with improved visibility. The single image also showed that different energy levels yield different information, thus supporting the dual energy analysis. The dual energy processing without water in the phantom showed that the MatLab tone mapping algorithm performed the best in improving the HDR image.

The dual energy HDR analysis with water in the phantom showed that, with the increased attenuation, HDR methods are unable to enhance the C7/T1 junction. However, it does show the impact of EV selection.

The dual energy HDR images with water in the phantom were then further processed for the regions of interest, namely the thoracic and cervical regions. The thoracic results showed no improvement or enhancement of the junction. The cervical results showed an enhancement and an SNR analysis was performed. The SNR results confirmed the effect of EV selection and it also showed that the image with the highest SNR is produced with an energy combination of 100 - 120 kV at EVs [-8; 0; 8].

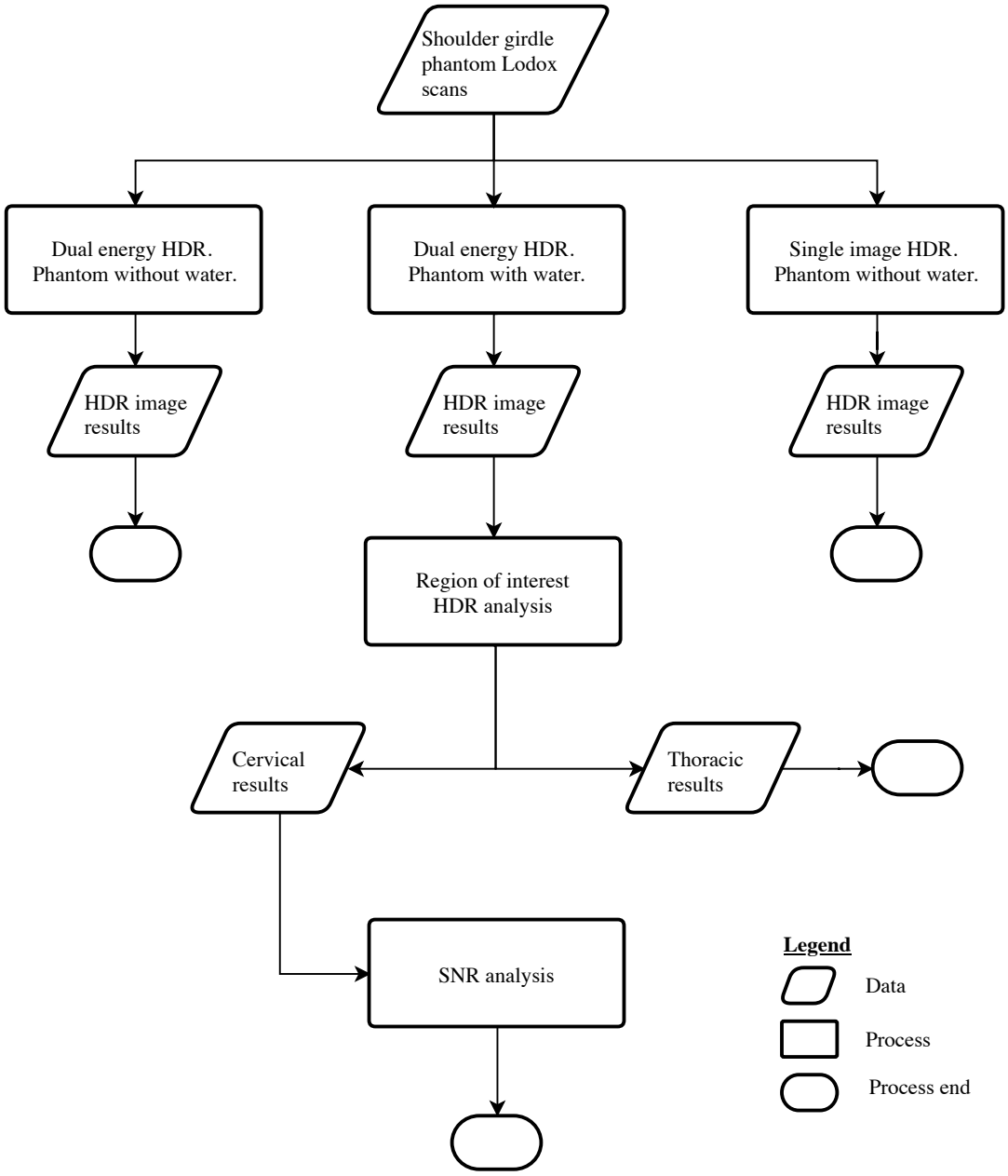

Figure 4.29: Sequence and processing of the exploration of the C7/T1 junction using HDR tone mapping.

Chapter 5

Conclusions

HDR techniques were implemented on single and dual energy X-ray images. The single image HDR exploration showed that X-rays at different energy levels reveal different levels of information - as expected. However, it showed that a single image was unable to reveal any further information of the C7/T1 junction after HDR processing and tone mapping.

The best performing tone mapping algorithm was the built-in MatLab algorithm which is an enhanced Ward histogram adjustment approach. Despite the various tone mapping algorithms, the dual energy HDR approach did not enhance the visualisation of the C7/T1 junction. However, it did show the impact of the exposure values on the visual appearance of the images.

The region of interest approach was taken from the dual energy HDR technique to further explore the thoracic and cervical regions individually. This approach shows that the thoracic region was not enhanced using HDR techniques to improve visibility of the C7/T1 junction. The cervical region results did visualise the vertebrae.

The HDR techniques applied on the single and dual energy X-ray images did not improve or enhance the visualisation of the C7/T1 junction

The study was limited to the tone-mapping algorithms discussed in Banterle et al. (2011). Furthermore, the phantom created bands of varying attenuation, reducing the image quality. The study only focused on exploring the C7/T1 junction in lateral radiographs and not other views.

5.1 Recommendations

Further HDR image construction techniques could be explored. A possible approach would be to use coloured multi-exposure images to create the HDR image, as shown to be feasible by Eppenberger et al. (2016). This could be applied within the dual energy approach to create the HDR image to be tone mapped.

The tone-mapping algorithms could also be expanded to include algorithms that aren't restricted by local or global parameters. Pendu et al. (2015) use a scalable image coding scheme that imposes no restriction to global or local operators by using block-wise and non-linear approaches. This approach could be applied to the HDR images to further explore its effect on the C7/T1 junction.

Other recommendations include using a cadaver in place of the phantom for acquisition of more realistic images. The ROI images could be extended to include all energy combinations to provide an exhaustive exploration. And finally, the effect of EVs could analysed by extending and reducing the different values assigned to each image i.e. a smaller or greater difference between each EV set.

The project has shown that SNR improvement using HDR tone mapping is possible, particularly for cervical scans. A future project could explore the effect of HDR and tone mapping on commonly performed X-ray examinations to assess possible enhancements in comparison to the available X-ray image visualisation tools.

References

Ahmad, N. (2003). *X-ray Patient Positioning Manual*.

Bandoh, Y., Qiu, G., Okuda, M., Daly, S., Aach, T., and Oscar, C. A. (2010). Recent advances in high dynamic range imaging technology. *Proceedings of 2010 IEEE 17th International Conference on Image Processing*, pages 3125–3128.

Banterle, F., Artusi, A., Debattista, K., and Chalmers, A. (2011). *Advanced High Dynamic Range Imaging: Theory and Practice*. AK Peters (CRC Press), Natick, MA, USA.

Bushberg, J. T., Seibert, J. A., Edwin M Leidholt, J., and Boone, J. M. (2002). *The Essential Physics of Medical Imaging Second Edition*. Lippincott Williams and Wilkins.

Carlsson, C. A. and Carlsson, G. A. (1996). *Basic physics of X-ray imaging*. Report/Linkpings hgskola, Institutionen fr radiologi.

Como, J. J., Leukhardt, W. H., Anderson, J. S., Wilczewski, P. A., Samia, H., and Claridge, J. A. (2011). Computed tomography alone may clear the cervical spine in obtunded blunt trauma patients: A prospective evaluation of a revised protocol. *Journal of Trauma, Injury, Infection and Critical Care*, 70(2):345–351.

Dahari, R. and Spitzer, H. (1996). Spatiotemporal adaptation model for retinal ganglion cells. *Journal of the Optical Society of America*, 13:419–435.

Debevec, P. E. and Malik, J. (1997). Recovering high dynamic range radiance maps from photographs. *Proc. of SIGGRAPH 97 Computer Graphics Proc*, pages 369–378.

Devlin, K. (2002). A review of tone reproduction techniques. Technical Report CSTR-02-005, Department of Computer Science, University of Bristol.

DICOM (2014). Digital imaging and communications in medicine. Online. http://dicom.nema.org/.

Eppenberger, P., Marcon, M., Ho, M., Grande, F. D., Frauenfelder, T., and Andreisek, G. (2016). Application of a colored multiexposure high dynamic range technique to radiographic imaging: an experimental trial to show feasibility. *Zurich Open Repository and Archive, University of Zurich*, 39:658–662.

Evangelopoulos, D. S., Deyle, S., Zimmermann, H., and Exadaktylos, A. K. (2011). Full-body radiography (lodox statscan) in trauma and emergency medicine: a report from the first european installation site. *Trauma*, 13:5–15.

Fell, M. (2010). Cervical spine trauma radiographs: Swimmers and supine obliques; an exploration of current practice. *Journal of Radiography*, 17:3–38.

Florea, C., Vertan, C., and Florea, L. (2007). Logarithmic model-based dynamic range enhancement of hip x-ray images. *Advanced Concepts for Intelligent Vision systems*, pages 587–596. ACIVS 2007.

France, J. C., Bono, C. M., and Vaccaro, A. R. (2005). Initial radiographic evaluation of the spine after trauma: When, what, where, and how to image the acutely traumatized spine. *Journal of Orthopaedic Trauma*, 19:640–649.

Granados, M., Ajdin, B., Wand, M., Theobalt, C., Seidel, H.-P., and Lensch, H. P. A. (2010). Optimal hdr reconstruction with linear digital cameras. *IEEE Computer Society Conference on Computer Vision and Pattern Recognition*, pages 215–222.

Gulam, M., Thornton, M. M., Hodsman, A. B., and Holdsworth, D. W. (2000). Bone mineral measurement of phalanges: Comparison of radiographic absorptiometry and area dual x-ray absorptiometry. *Radiology*, 216(2):586–591.

Hubbel, J. and Seltzer, S. (2009). Tables of x-ray mass attenuation coefficients and mass energy-absorption coefficients from 1 kev to 20 mev for elements z = 1 to 92 and 48 additional substances of dosimetric interest. Online. last updated December 2011: http://www.nist.gov/pml/data/xraycoef/.

Ishikawa, H., Chen, C.-L., Wollstein, G., Grimm, J. L., Ling, Y., Bilonick, R. A., Sigal, I. A., Kagemann, L., and Schuman, J. S. (2013). High dynamic range imaging concept-based signal enhancement method reduced the optical coherence tomography measurement variability. *Investigative Ophthalmology & Visual Science*, 54:836 – 841.

Kanelovitch, L., Itzchak, Y., Rundstein, A., Sklair, M., and Spitzer, H. (2013). Biologically derived companding algorithm for high dynamic range mammography images. *IEEE Transactions on Biomedical Engineering*, 60(8):2253 – 2261.

Kulaylat, A. N., Tice, J. G., Levin, M., Kunselman, A. R., Methratta, S. T., and Cilley, R. E. (2012). Reduction of radiation exposure in pediatric patients with trauma:

cephalic stabilization improves adequacy of lateral cervical spine radiographs. *Journal of Pediatric Surgery*, 47:984 – 990.

Lakshmi, S. V., Janet, J., Sujathi, S., and Bellarmine, T. (2012). Analysis of tone mapping operators on high dynamic range images. *Proceeding of the 2012 Southeastcon*, pages 1–6.

Larson, G. W., Rushmeier, H., and Piatko, C. (1997). A visibility matching tone reproduction operator for high dynamic range scenes. *IEEE Transactions on Visualization and Computer Graphics*, 3(4):291–306.

Lischinski, D., Farbman, Z., Uyttendaele, M., and Szeliski, R. (2006). Interactive local adjustment of tonal values. *ACM Transactions on Graphics (TOG) - Proceedings of ACM SIGGRAPH*, 25:646–653.

Mann, S. and Picard, R. (1994). On being 'undigital' with digital cameras: Extending dynamic range by combining differently exposed pictures. Technical Report 323, MIT Media Lab Perceptual Computing Section, Boston, Massachusetts.

MathWorks (2017). Mathworks: Matlab image processing toolbox function tonemap. Online. Last accessed: 7 February 2017: http://www.mathworks.com.au/help/toolbox/images/ref/tonemap.html.

Mazess, R. B., Barden, H. S., Bisek, J. P., and Hanson, J. (1990). Dual-energy x-ray absorptiometry for total-body and regional bone-mineral and soft-tissue composition. *The American Journal of Clinical Nutrition*, 51:1106 – 1112.

Meylan, L. (2006). High dynamic range image rendering with a retinex-based adaptive filter. *IEEE Transactions on Image Processing*, 15(9):2820 – 2830.

Mitsunaga, T. and Nayer, S. K. (1999). Radiometric self calibration. *IEEE Conf. on Computer Vision and Pattern Recognition*, 1:374–380.

Mullin, T. I., Wang, M., and Rao, R. D. (2013). Radiographic characterization of prevertebral soft tissue shadow in the cervicothoracic region of normal adults. *Journal of Surgical Research*, 180:73–79.

Necsa (2012). necsa today - official newsletter of necsa. Issue 2.

Parizel, P. M., van der Zijden, T., Gaudino, S., Spaepen, M., Voormolen, M. H. J., Venstermans, C., Belder, F. D., van den Hauwe, L., and Goethem, J. V. (2009). Trauma of the spine and spinal cord: imaging strategies. *European Spine Journal*, 19:S8S17.

Patrascu, V., Buzuloiu, V., and Vertan, C. (2003). *Fuzzy image enhancement in the framework of logarithmic model*, volume 122, pages 219 – 237. Springer Verlag, Heidelberg.

Pendu, M. L., Guillemot, C., and Thoreau, D. (2015). Local inverse tone curve learning for high dynamic range image scalable compression. *IEEE Transactions on Image Processing*, 24:5753–5763.

Pitcher, R. D., van As, A. B., Sanders, V., Douglas, T. S., Wieselthaler, N., Vlok, A., Paverd, S., Kilborn, T., Rode, H., Potgieter, H., and Beningfield, S. J. (2008). A pilot study evaluating the statscan digital x-ray machine in paediatric polytrauma. *Emergency Radiology*, 42:35–42.

Potgieter, J., de Villiers, M., Scheelka, M., and de Jager, G. (2005). An explanation for extremely low, but variable radiation dosages measured in linear slit scanning radiography system. *Medical Imaging 2005: The Physics of Medical Imaging, Proceedings of the SPIE*, 5745:1138–45.

Prakel, D. (2009). *Basics Photography 07: Exposure*. AVA Publishing.

Reinhard, E. (2003). Parameter estimation for photographic tone reproduction. *Journal of Graphics Tools*, 7(1):45–51.

Reinhard, E., Stark, M., Shirley, P., and Ferwerda, J. (2002). Photographic tone reproduction for digital images. *In SIGGRAPH 2002 Conference Proceedings*.

Reinhard, E., Ward, G., Pattanaik, S., and Debevec, P. (2006). *High Dynamic Range Imaging: Acquisition, Display and Image Based Lighting*. Morgan Kaufmann.

Rethnam, U., Yesupalan, R. S., and Bastawrous, S. S. (2008). The swimmer's view: does it really show what it is supposed to show? a retrospective study. *BMC Medical Imaging*, 8:2.

Robertson, M., Borman, S., and Stevenson, R. (2003). Estimation-theoretic approach to dynamic range enhancement using multiple exposures. *Journal of Electronic Imaging*, 12:219–228.

Sakmann, B. and Creutzfeldt, O. D. (1969). Scotopic and mesopic light adaptation in the cats retina. *Pflugers Archiv European Journal of Physiology*, 313:168–185.

Salih, Y., bt. Md-Esa, W., Malik, A. S., and Saad, N. (2012). Tone mapping of hdr images: A review. *4th International Conference on Intelligent and Advanced Systems*, 1:368– 373.

Sisniega, A., Abella, M., Desco, and Vaquero, J. (2014). Dual-exposure technique for extending the dynamic range of x-ray flat panel detectors. *Physics in Medicine and Biology*, 59(2):421 – 439.

StatsSa (2018). Mortality and causes of death in south africa, 2016:findings from death notification. Technical report, Statistics South Africa.

Stein, D. M., Ishikawa, H., Hariprasad, R., Wollstein, G., Noecker, R. J., Fujimoto, J. G., and Schuman, J. S. (2006). A new quality assessment parameter for optical coherence tomography. *British Journal of Ophthalmology*, 90:186–190.

Svendsen, O. L., Haarbo, J., Hassager, C., and Christiansen, C. (1993). Accuracy of measurements of body composition by dual-energy x-ray absorptiometry in vivo. *The American Journal of Clinical Nutrition*, 57:605–608.

Trpovski, Z., Kerkez, V., and Vucinic, P. (2013). Hdr processing for legibility enhancement of radiographic images. *First International Conference and SME Workshop on HDR imaging*, 1(6).

Webb, P. (2008). Rendering high dynamic range images on the web. MATLAB Digest.

Wheeless, C. R. (2011). Oblique view of c spine. online. Last updated Thursday, August 25, 2011 1:53 pm. Last accessed 31 July 2013.

Yoshida, A., Blanz, V., Myszkowski, K., and Seidel, H.-P. (2005). Perceptual evaluation of tone mapping operators with real-world scenes. *Human Vision & Electronic Imaging X, SPIE*, pages 192–203.